



HOMESTAKE MINING CO.
1375 Greg Street, Suite 105
Sparks, NV 89431

MAY 3 1994

888188

Geological Survey Branch
MEMPR

April 26, 1994

Tom Schroeter
Senior Regional Geologist
Province of British Columbia Ministry of Energy, Mines and Petroleum Resources
Geological Survey Branch
Suite 301 - 865 Hornby Street
Vancouver, B.C. V6Z 2G3

Dear Tom,

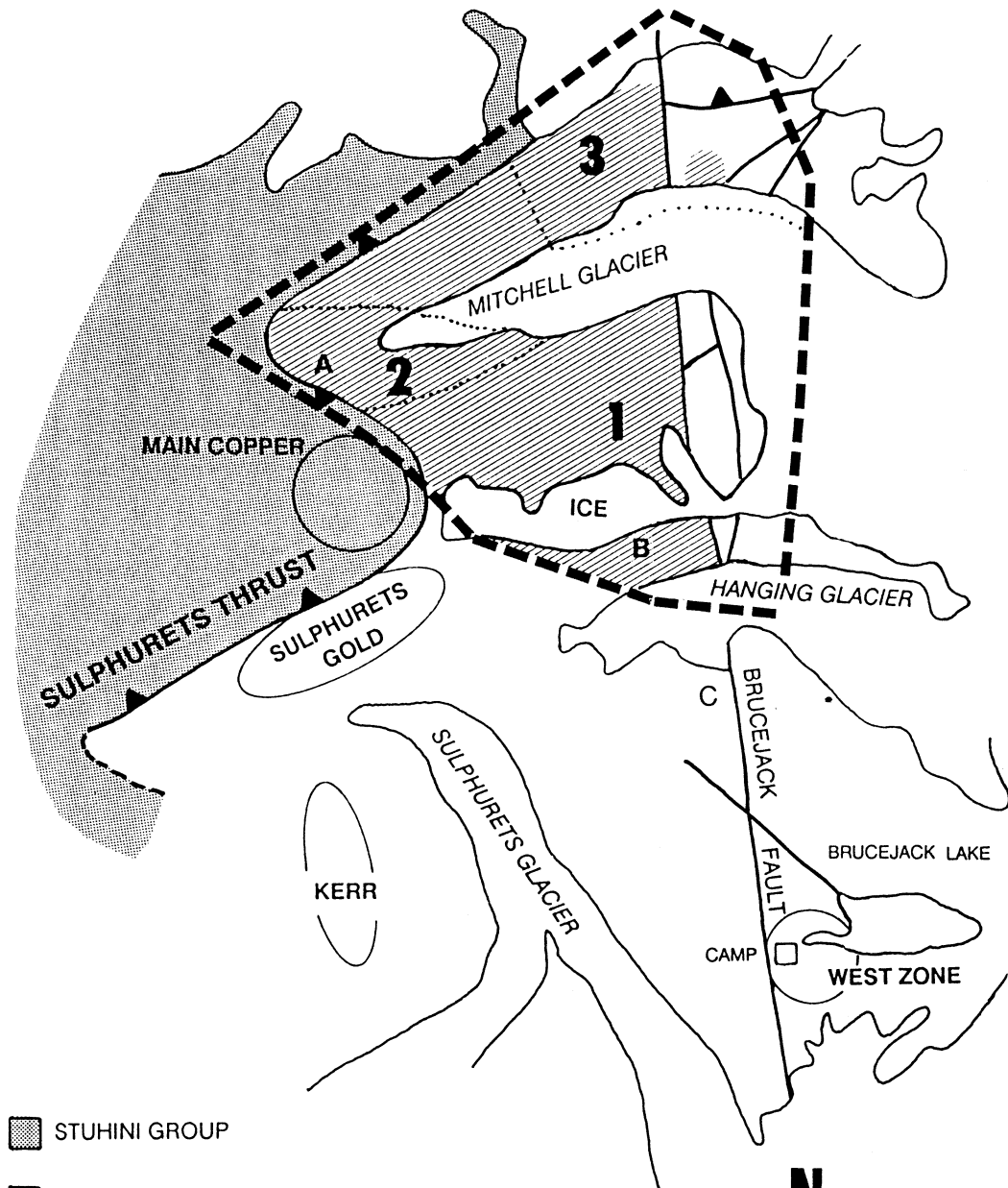
Enclosed is my dissertation on Sulphurets on disk formatted in wordperfect (IBM). Also enclosed are the hard copy figures with captions.


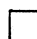



If you have problems with the disk or format, please contact me.

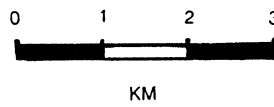
Best Regards,

Jacob Margolis

FIGURE 1. Generalized map of the Sulphurets district; geology from Britton and Alldrick (1988); study area outlined by heavy dashed line; dotted lines in study area mark the three subdistricts as discussed in the text: 1, Snowfield (number placed at location of Snowfield gold zone); 2, Mitchell (number placed at Mitchell stockwork zone); and 3, Iron Cap (number placed at pyrite vein area); "A" = Alder zone, "B" = Josephine zone; Main Copper, Sulphurets Gold, Kerr, West Zone, and "C" (Goldwedge) are mineralized zones noted in the text.



-  STUHINI GROUP
-  HAZELTON GROUP
-  HYDROTHERMAL ALTERATION
WITHIN THE STUDY AREA
-  HIGH-ANGLE FAULT
-  THRUST FAULT
(teeth on upper plate)



**SULPHURETS DISTRICT
BRITISH COLUMBIA**

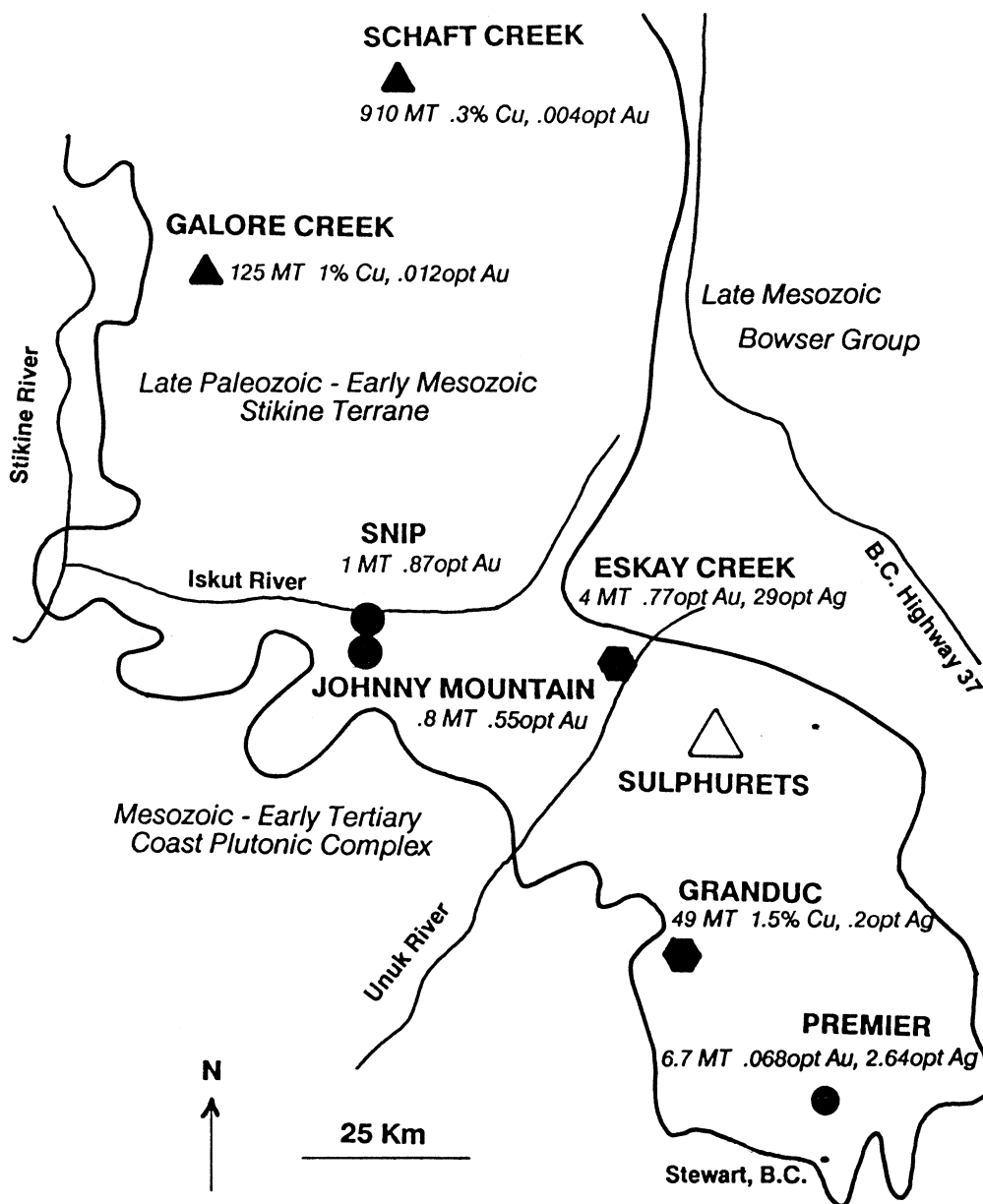


FIGURE 2. Mineralization in the Iskut region; data are in millions of tons (MT), except Eskay Creek (tonnes); opt = ounces per ton; data from Thorstad (1991), Grove (1986), and Roth and Godwin (1992); triangles are porphyry Cu-Au deposits, circles are epithermal or mesothermal vein deposits, and hexagons are volcanogenic massive sulfide deposits.

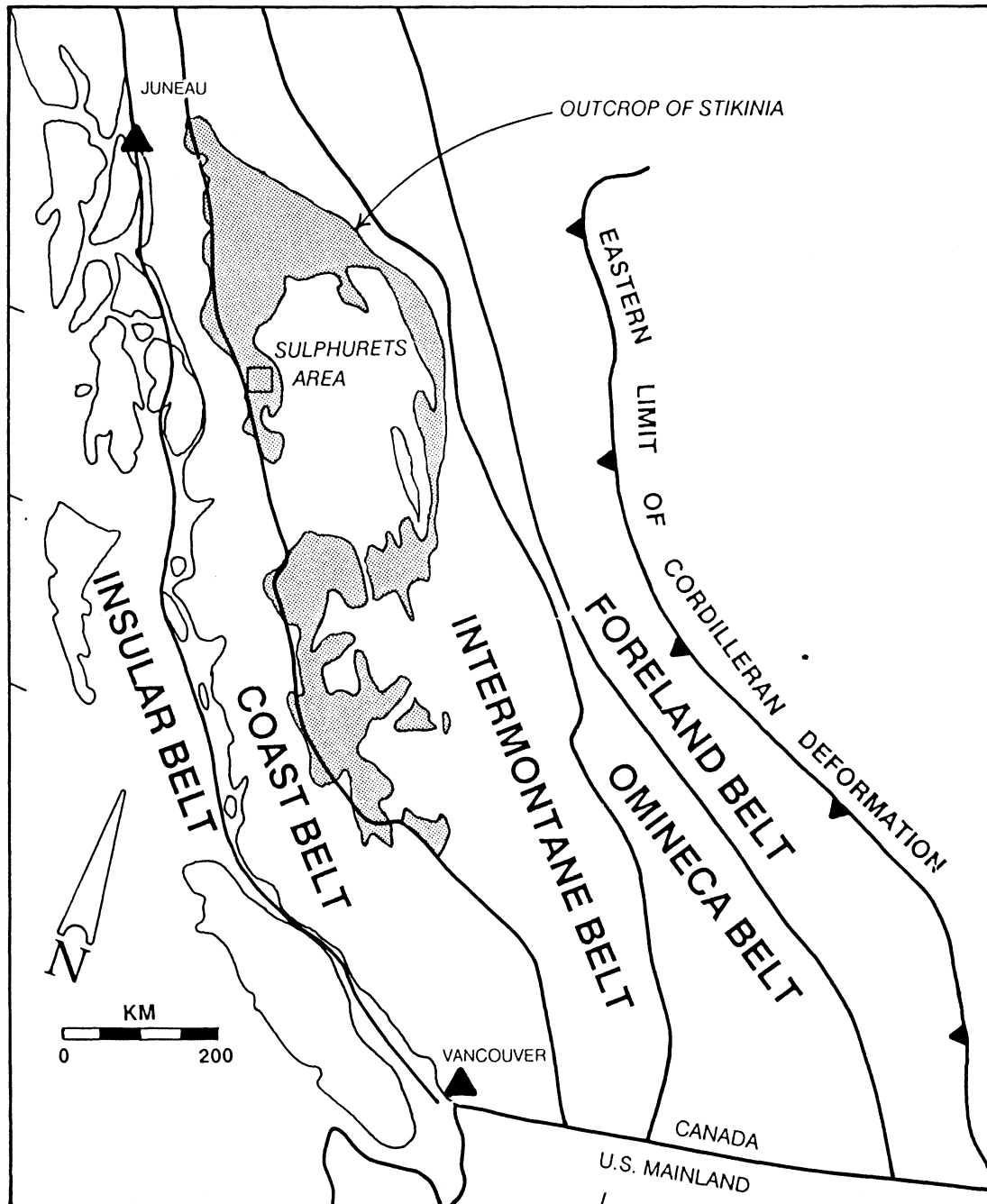


FIGURE 3. Regional setting of the Sulphurets district; from Evenchick (1991); sipped pattern is the outcrop area of Stikine terrane; box shows the location of the Sulphurets district.

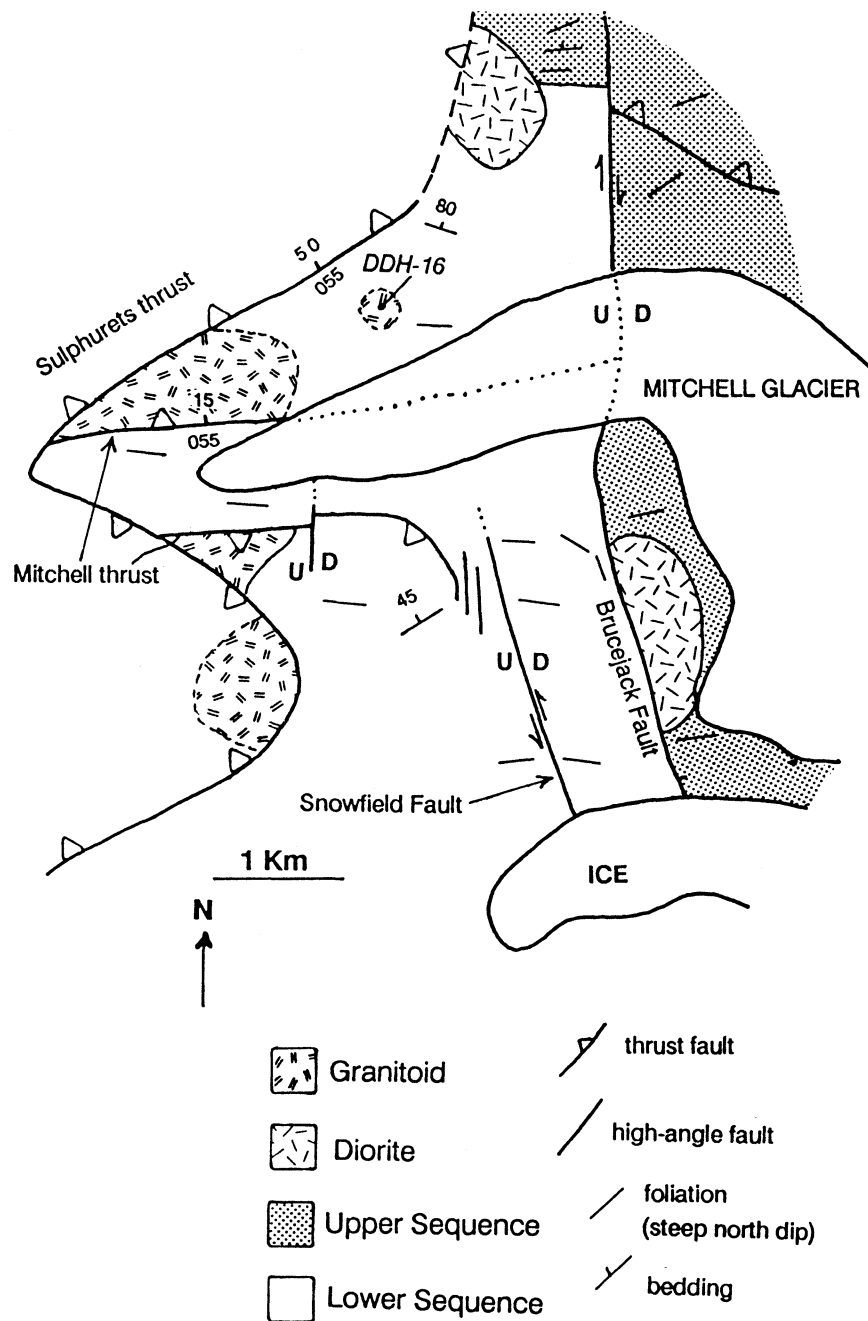


FIGURE 4. Generalized geologic map of the study area; data from this study and modified from Britton and Alldrick (1988); drill hole DDH-16 shown with granitoid in subsurface (see text); elevations increase north and south away from Mitchell Glacier.

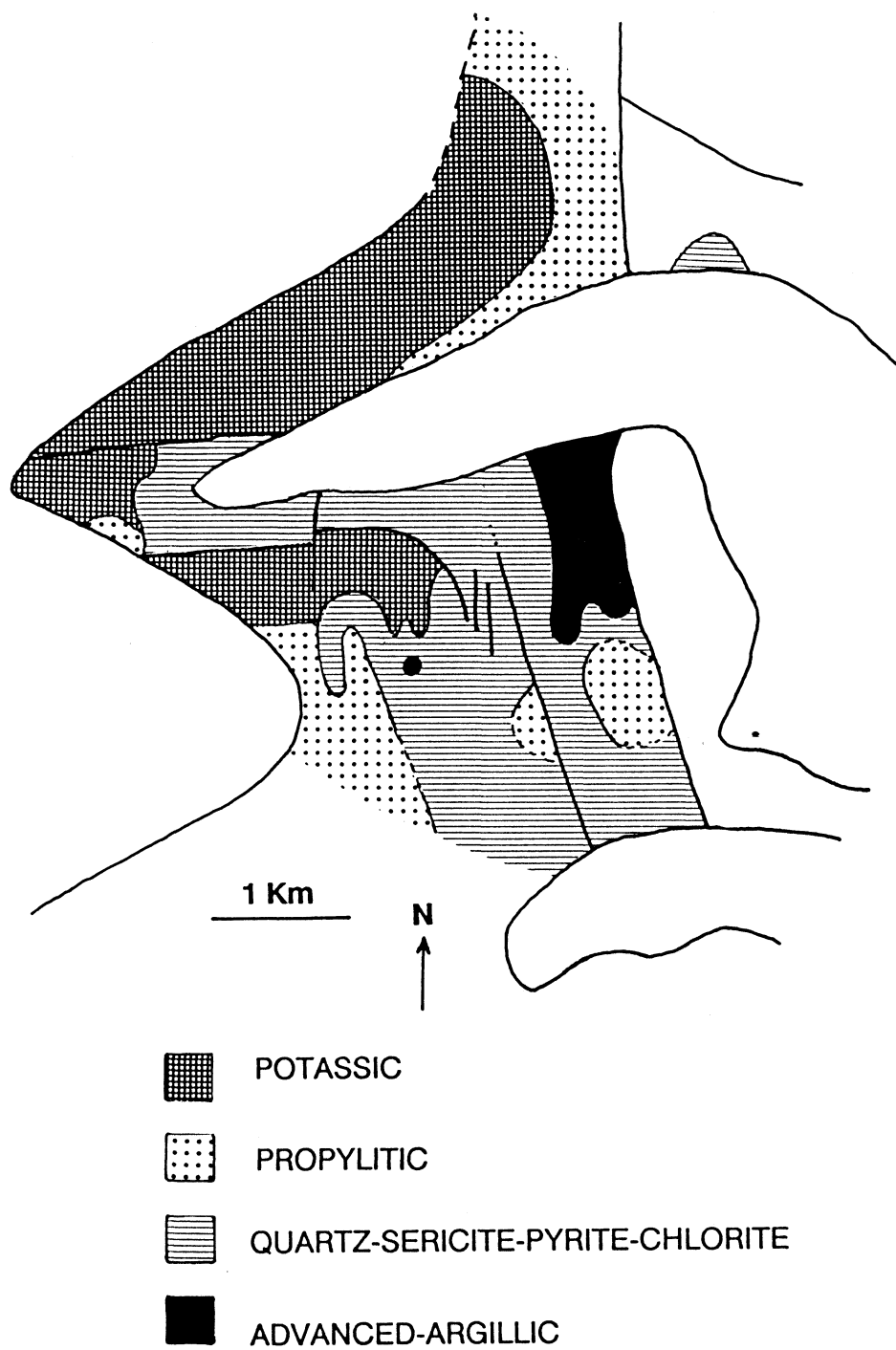


FIGURE 5. Generalized alteration map of the study area; refer to Fig. 4 for names of features.

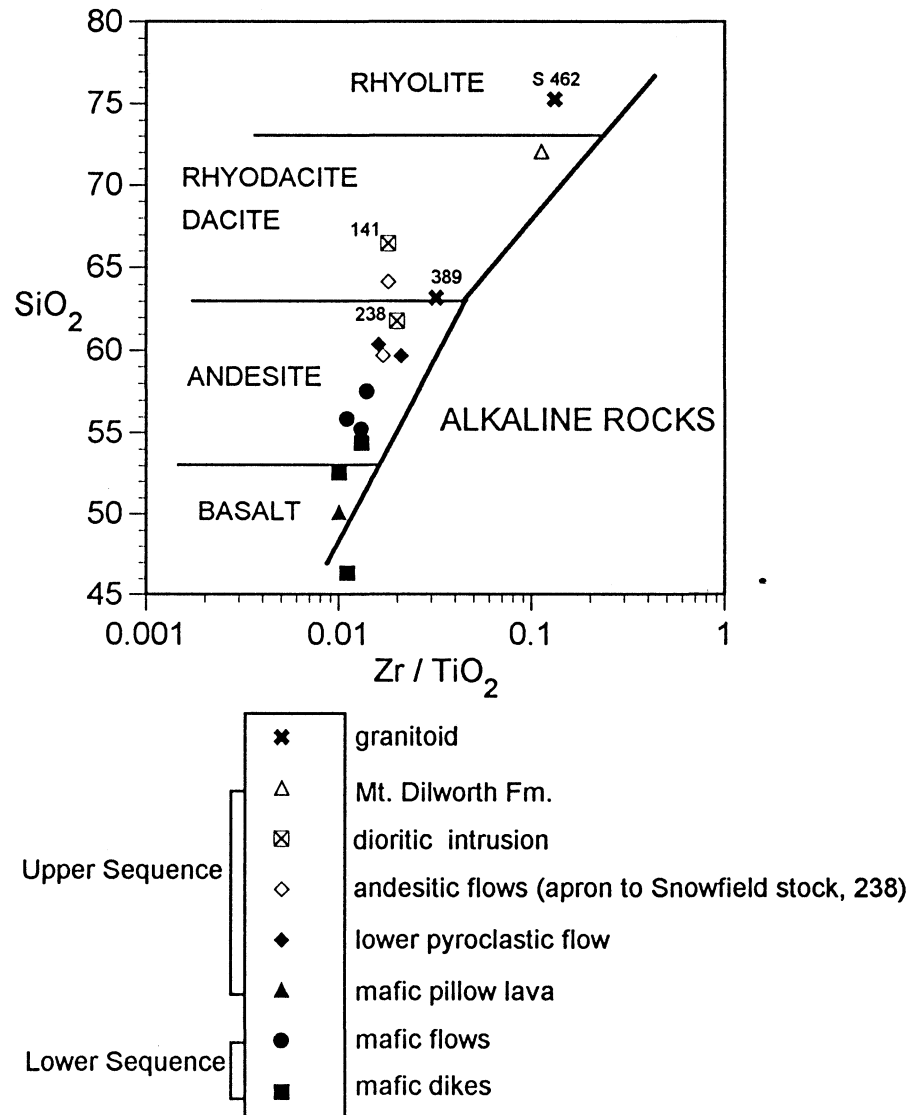


FIGURE 6. Composition of igneous rocks in the northern Sulphurets district following the method of Winchester and Floyd (1977); sample numbers are: 462, quartz-syenite; 141, Iron Cap stock; 389, monzonite in Main Copper area; 238, Snowfield stock.

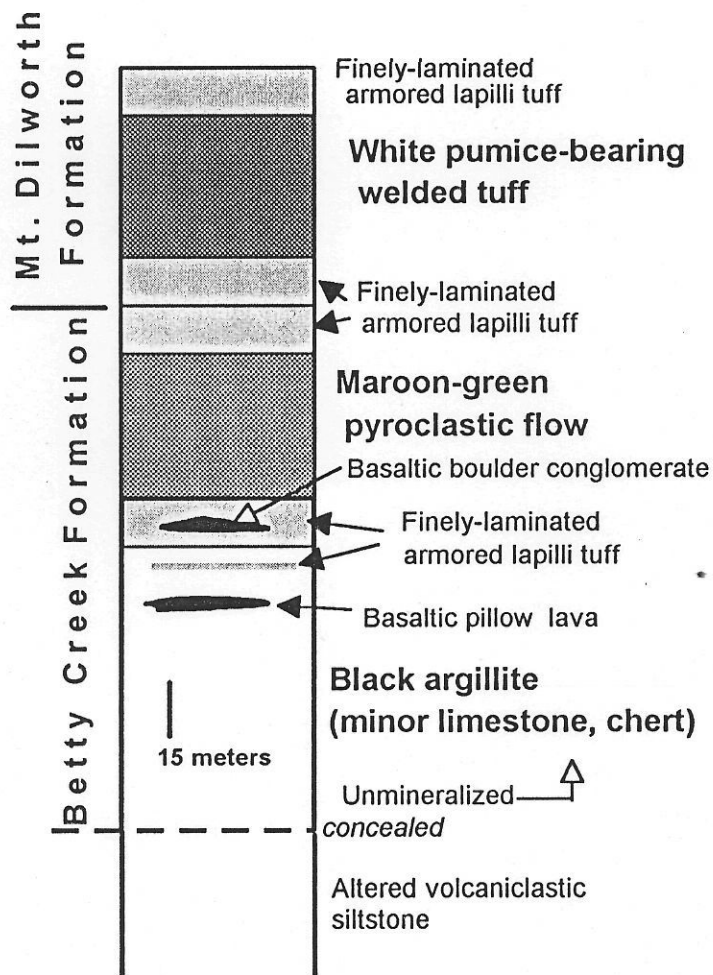


FIGURE 7. Generalized stratigraphic column of the Upper Sequence east of the Brucejack fault in the Iron Cap subdistrict as described in the text.

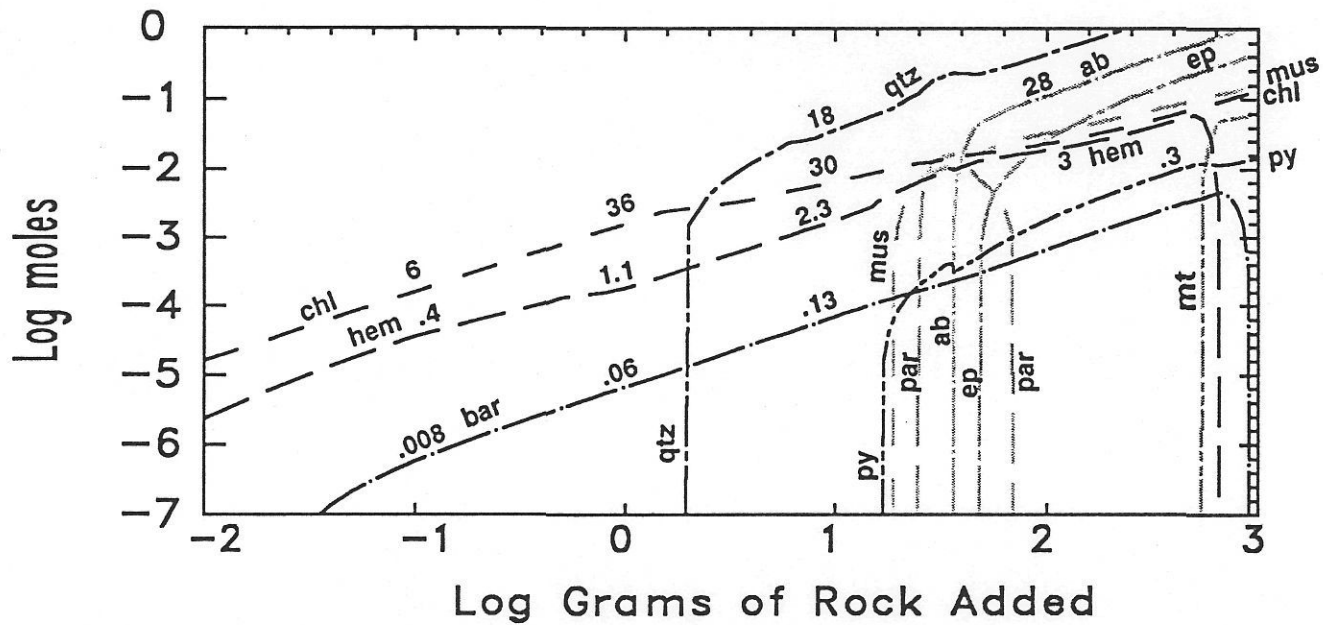


FIGURE 8. Results of numerical calculations of the reaction between seawater and andesite at 300°C as discussed in the section II A 3 (Table 3); the water-to-rock decreases from left to right, the right edge represents a ratio of 1; curves represent moles of a given mineral in the assemblage; numbers along curves are approximate weight-percent for selected minerals at points along the reaction; not all minerals are shown (see text); mineral abbreviations: chl, Mg-chlorite; hem, hematite; bar, barite; qtz, quartz; musc, muscovite; py, pyrite; par, paragonite; ab, albite; ep, epidote; mt, magnetite.

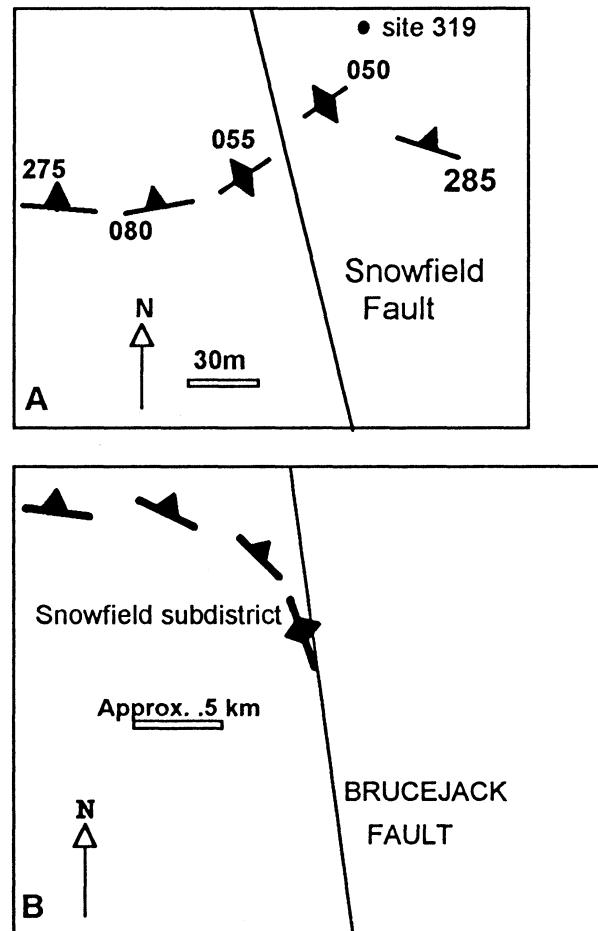


FIGURE 9. Sketches illustrating the rotation of foliations (heavy lines) adjacent to the Snowfield fault (a) and Brucejack fault (b); heavy lines are foliations, numbers indicate strike; all foliations are steep ($>60^\circ$), barbs point in dip directions, double barbs indicate vertical dip; no amount of offset is implied along the Brucejack fault.

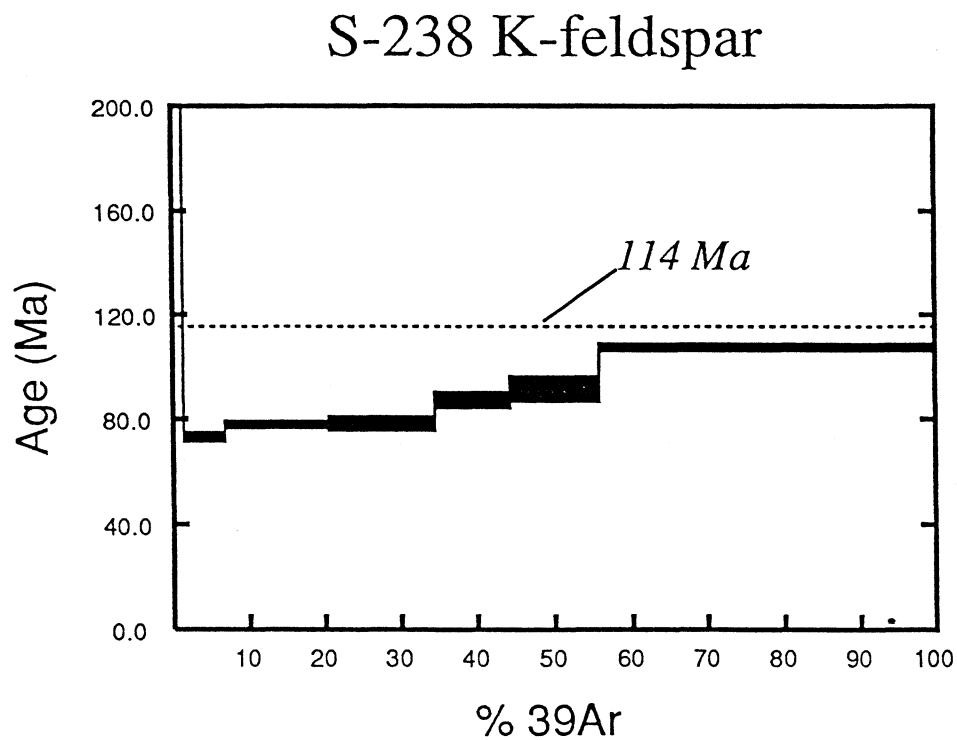


FIGURE 10. Argon plateau diagram for K-feldspar phenocrysts from the Snowfield diorite stock (sample 238); 114 Ma is estimate of age, since no multiple-step plateau is developed; values along the abscissa represent the percentage of ^{39}Ar released during each heating step, temperature of heating steps increasing from left to right; the thickness of each bar (step) is equal to twice the standard deviation about the mean age for the step (see Appendix C for data).

Tourmaline S-418

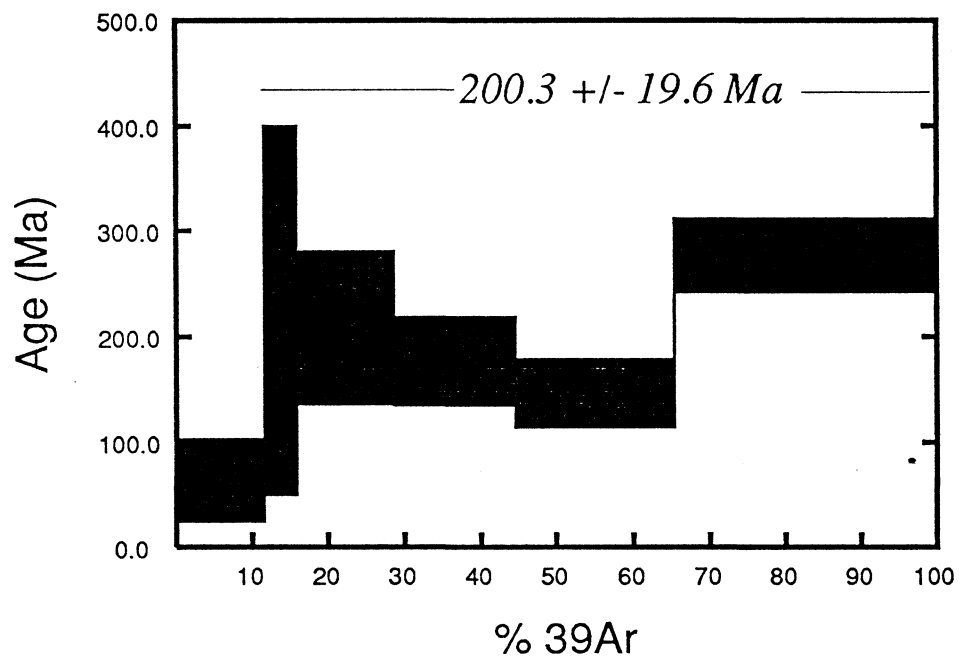


FIGURE 11. Argon plateau diagram for hydrothermal tourmaline in sericitic alteration; sample 418, west of Josephine zone; age of 200 ± 19.6 Ma is average of five higher temperature steps; see Figure 10 for further information.

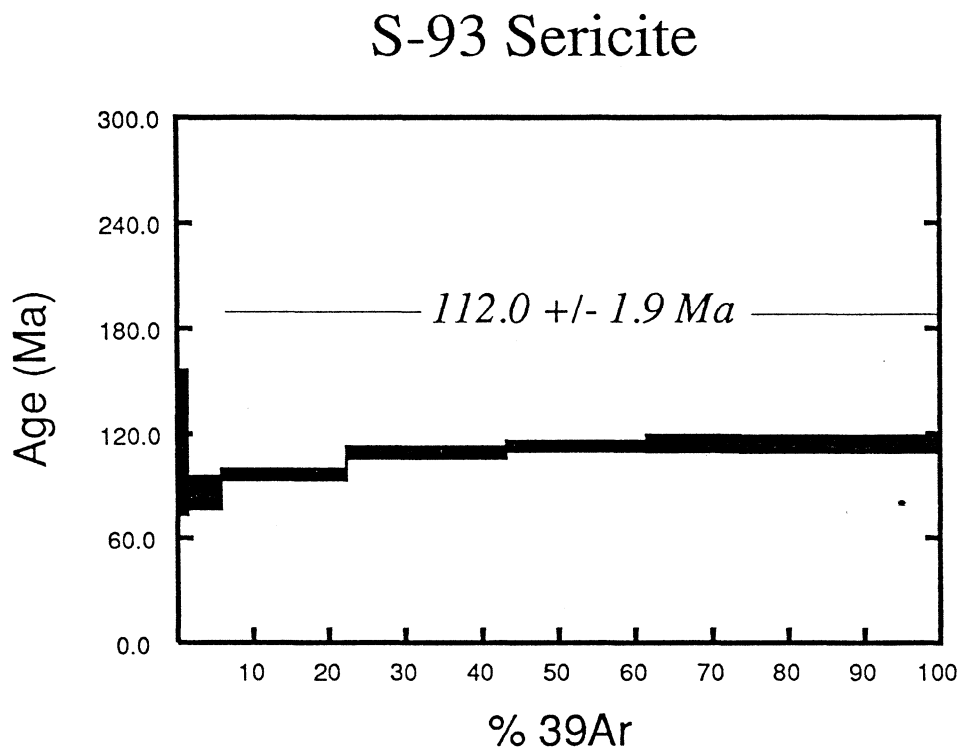


FIGURE 12. Argon plateau diagram for hydrothermal sericite from sericitic alteration containing molybdenite; sample 93, Mitchell subdistrict; age of 112 ± 1.9 Ma is average of four higher temperature steps; see Figure 10 for further information.

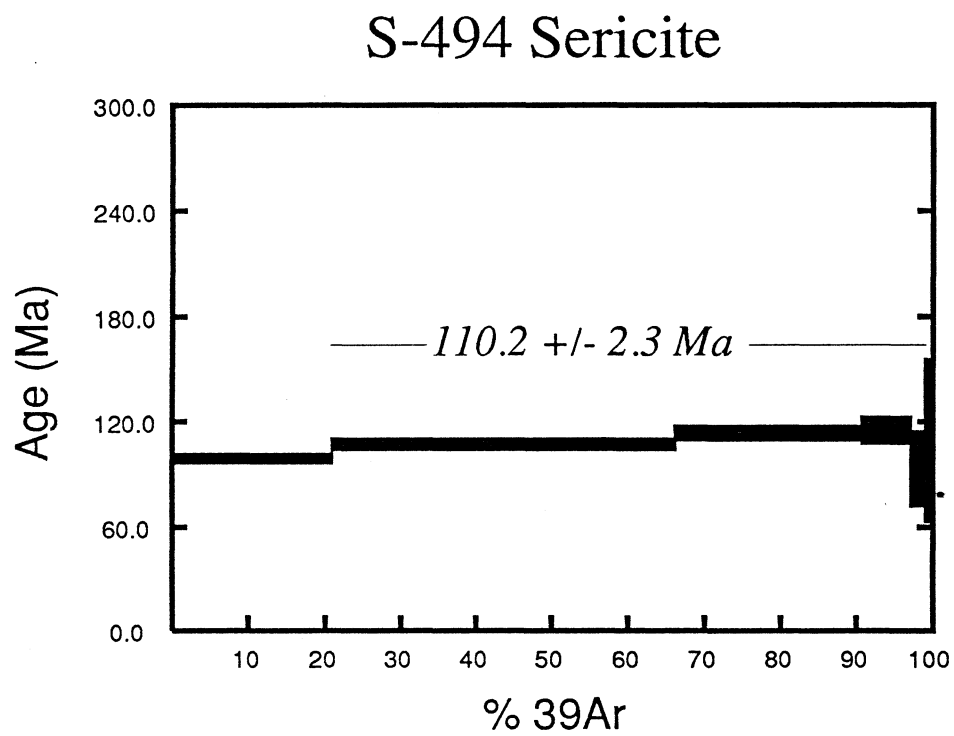


FIGURE 13. Argon plateau diagram for recrystallized sericite from pressure shadows adjacent to pyrite grains; sample 494, alteration surrounding the West zone vein area; age of $110.2 \pm 2.3 \text{ Ma}$ is average of five higher temperature steps; see Figure 10 for further information.

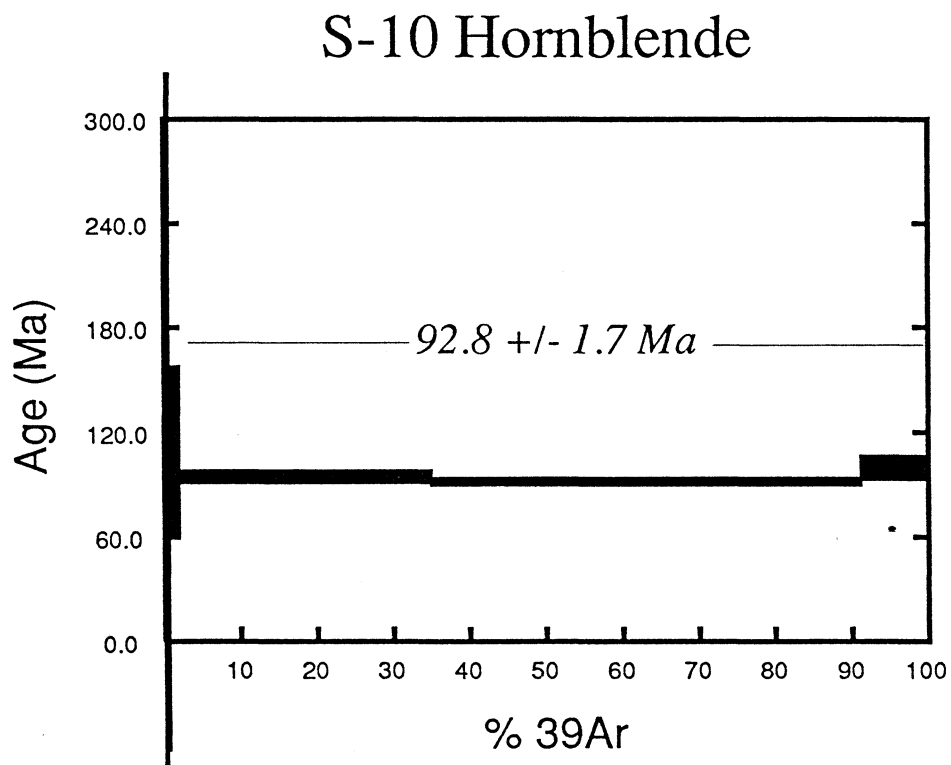


FIGURE 14. Argon plateau diagram for hornblende from a mafic dike in the Lower Sequence; sample 10, Snowfield subdistrict; age of 92.8 ± 1.7 Ma is average of three higher temperature steps; see Figure 10 for further information.

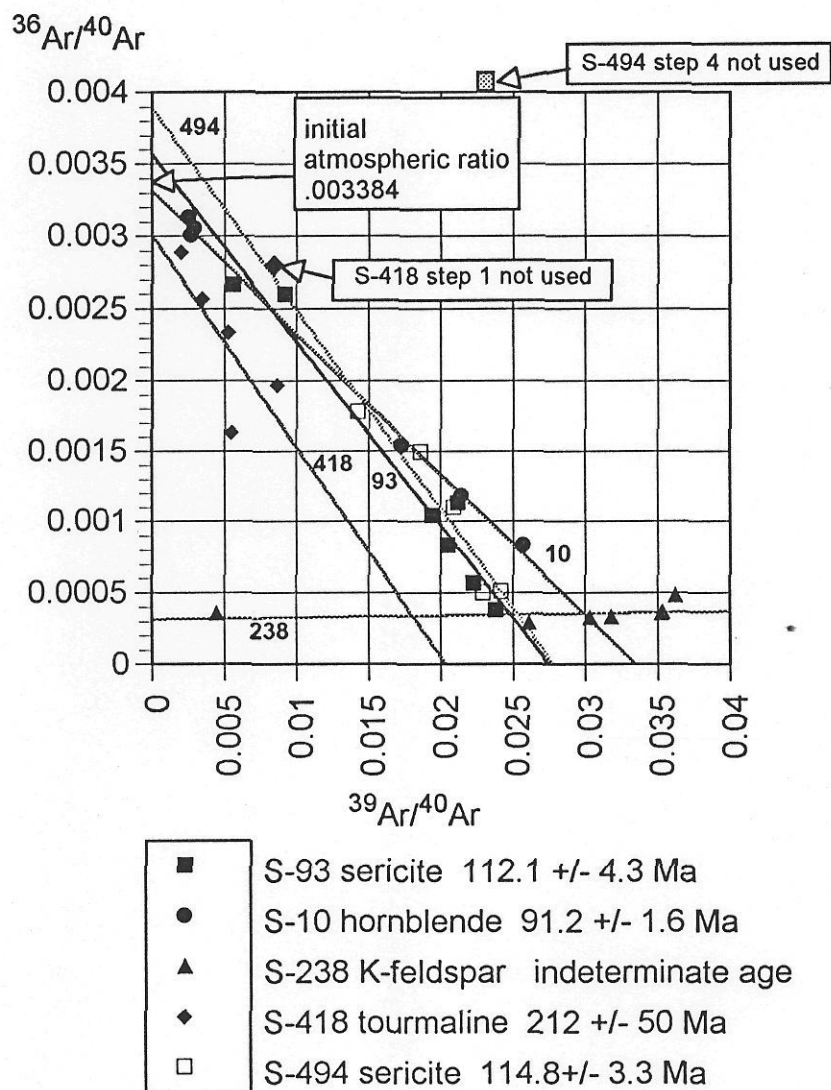


FIGURE 15. Inverse isochron plot for Ar-Ar data; ages shown in legend were calculated from the intercept of the isochron with the abscissa; note that the K-feldspar sample 238 forms an isochron which does not approach the atmospheric value (see text for discussion) and, therefore, provides no age information.

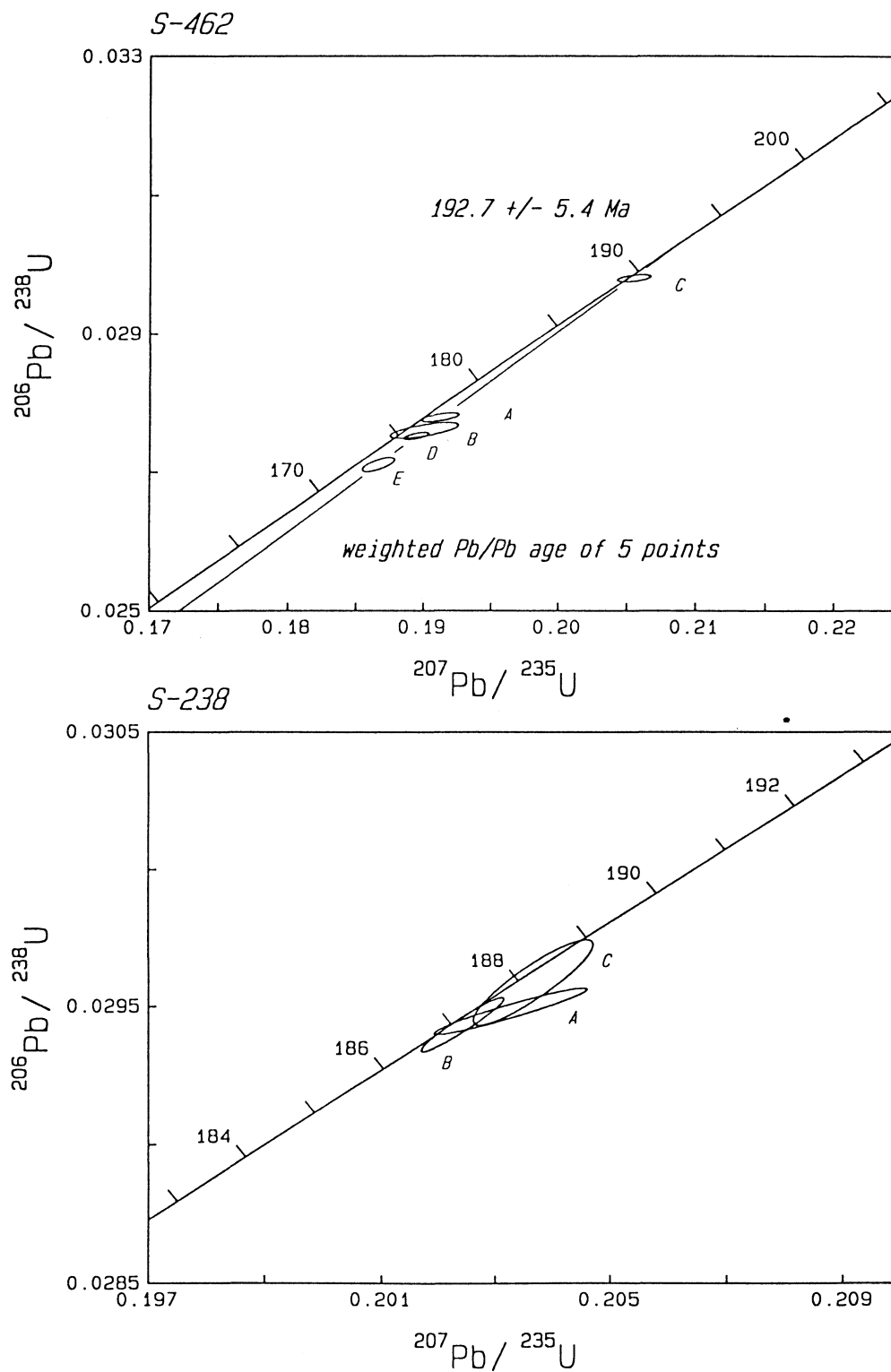


FIGURE 16. Concordia plots of U-Pb isotopic data obtained on zircon fractions from the Snowfield diorite stock (S238) and quartz-syenite (S462); ages in Ma are plotted along the concordia curves; see Appendix I for data and text for interpretation.

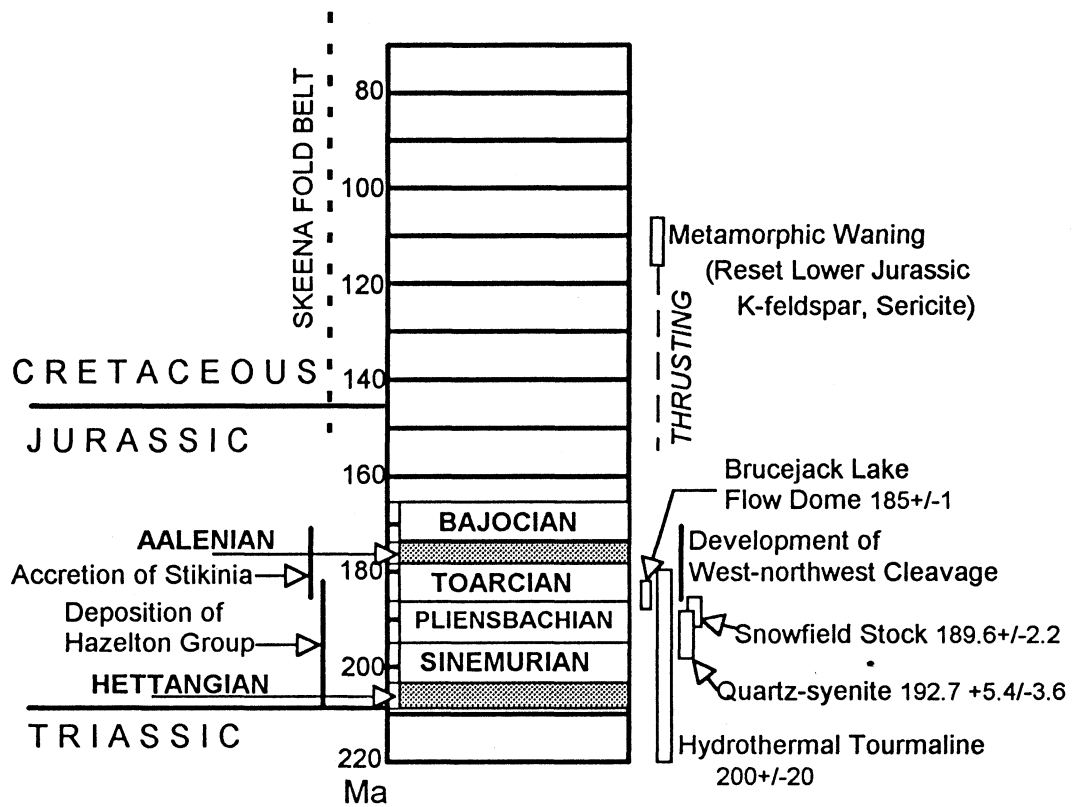


FIGURE 17. Time-scale summarizing geologic events related to the study area; stages plotted according to Harland et al. (1990); rectangles along right side correspond to the dates (including 2σ errors) obtained in this study, except for the Brucejack Lake flow dome (Macdonald, 1993); data along the left correspond to published information cited in the text.

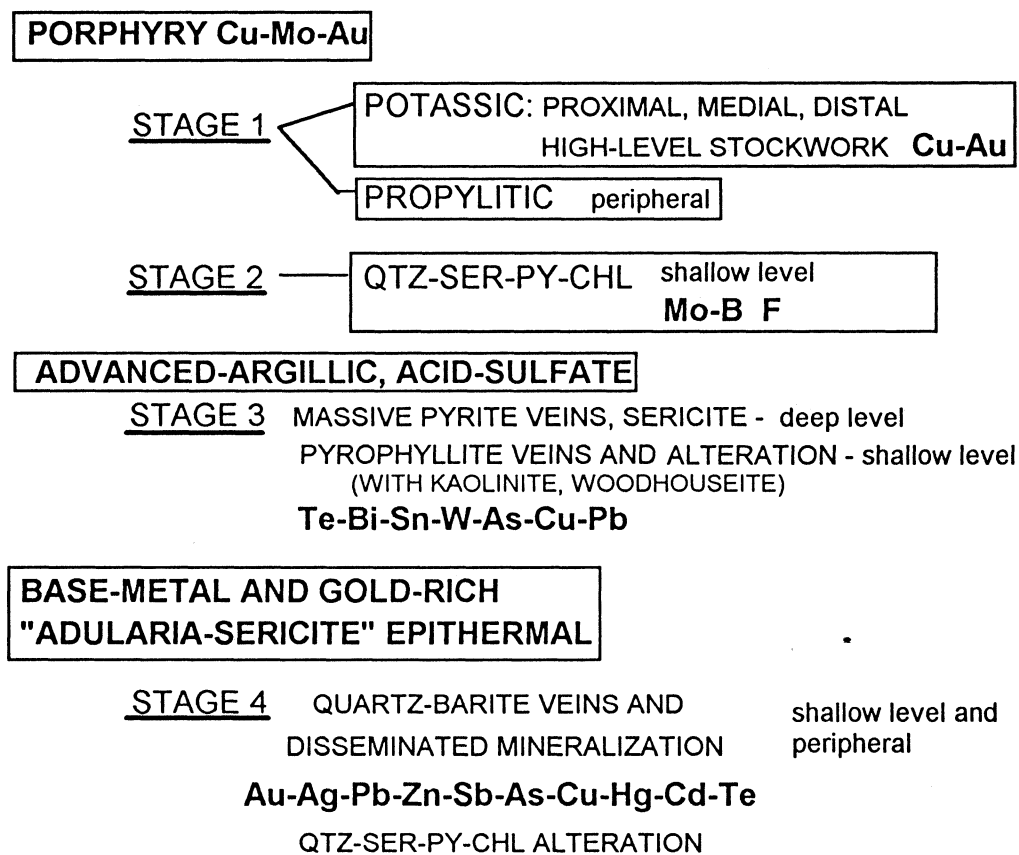


FIGURE 18. Diagram summarizing the four stages of hydrothermal alteration and related mineralization in the study area; QTZ-SER-PY-CHL is abbreviation for quartz-sericite-pyrite-chlorite.

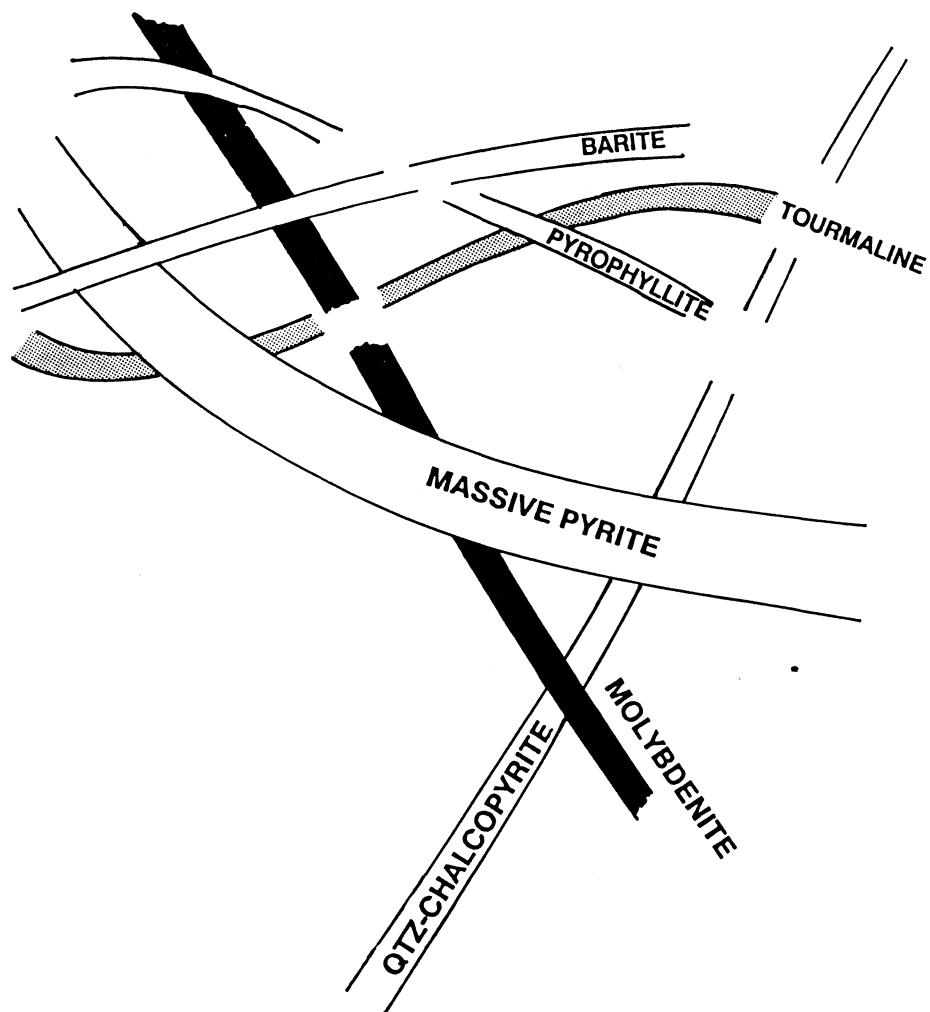
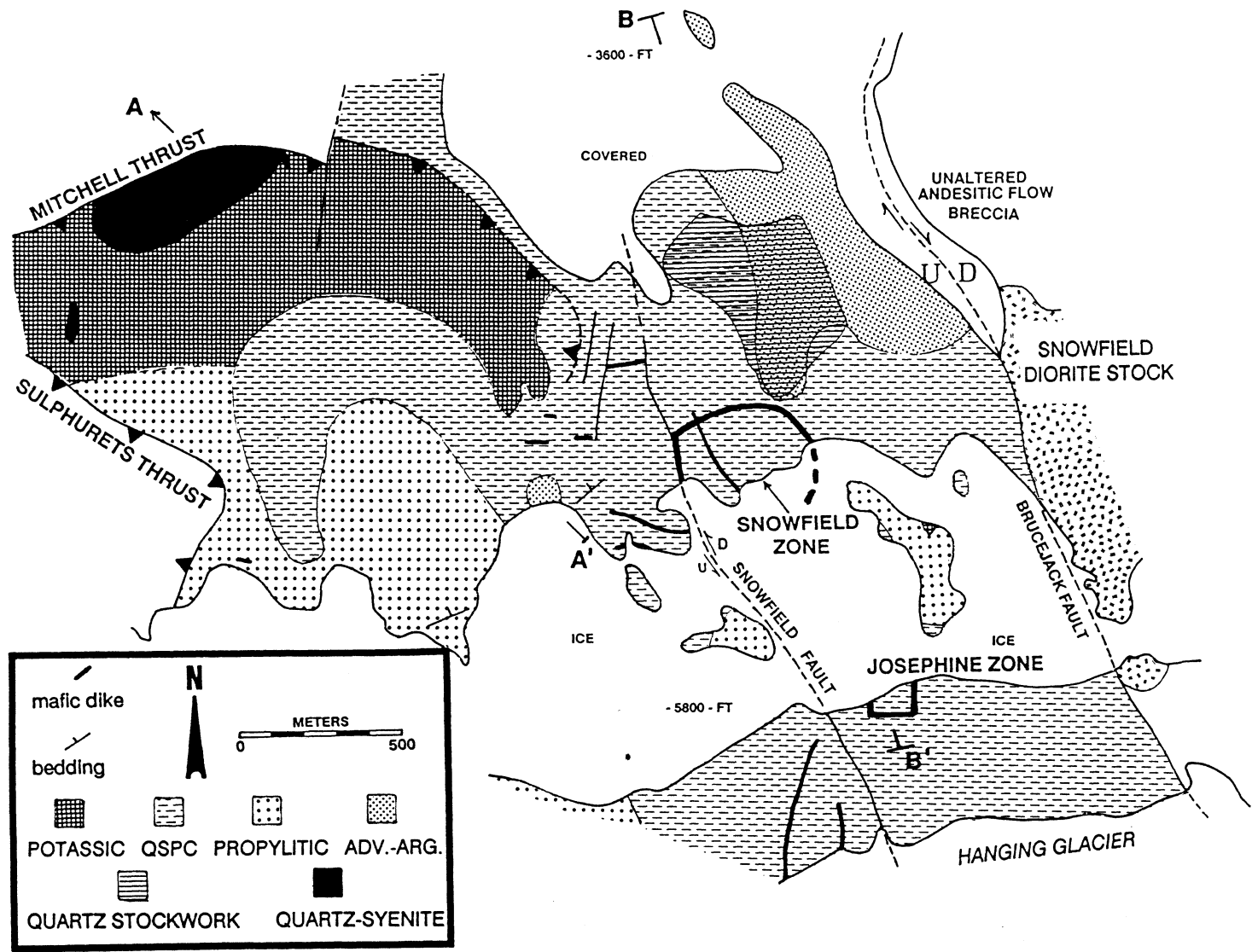


FIGURE 19. Cross-cutting relationships among vein types in the study area; intersections which show no relationship are those which were not observed; the diagram is not intended to reflect the actual spatial distribution of vein types; quartz-chalcopyrite veins correspond to stage 1, molybdenite and tourmaline to stage 2, massive pyrite and pyrophyllite to stage 3, and barite to stage 4.

FIGURE 20. Map showing the distribution of alteration in the Snowfield subdistrict; cross-sections A-A' and B-B' are shown in Figures 24 and 25, respectively; note the increasing elevation from the north side of the map (50 meters south of Mitchell Glacier) to the level of the Josephine vein zone; elevations then decrease south toward Hanging Glacier (see Figure 25); the Mitchell subdistrict is located northwest of the map area (see Figure 21); for orientation, the quartz-syenite is shown - it is potassically altered as are surrounding country rocks; abbreviations are - QSPC, quartz-sericite-pyrite±chlorite; ADV.-ARG., advanced-argillic.



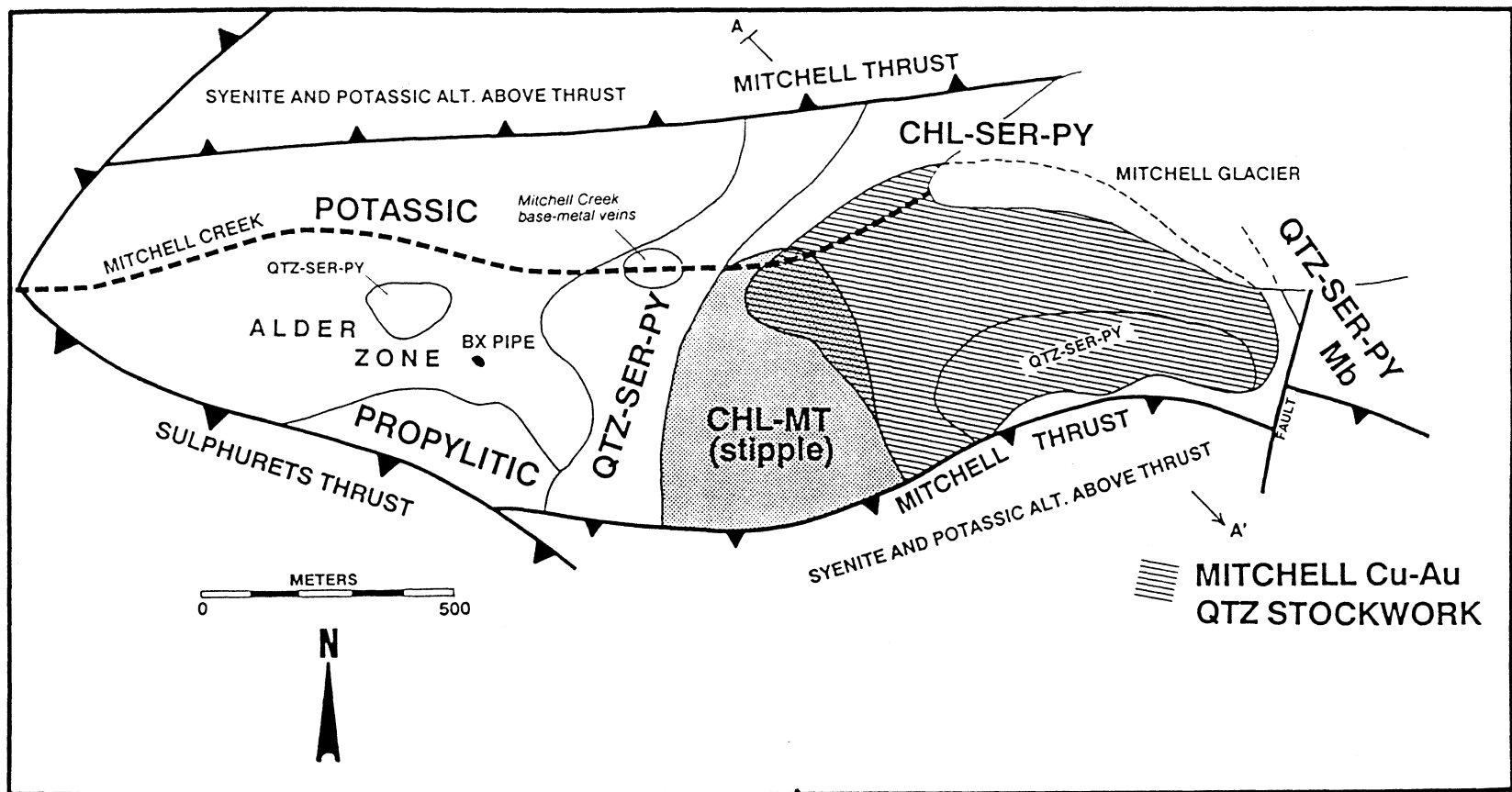


FIGURE 21. Map showing the distribution of hydrothermal alteration in the Mitchell subdistrict; abbreviations are: CHL-MT, chlorite-magnetite zone in CHL-SER-PY (chlorite-sericite-pyrite) alteration; QTZ-SER-PY, quartz-sericite-pyrite; Mb, molybdenite; cross-section A-A' is shown in Figure 24.

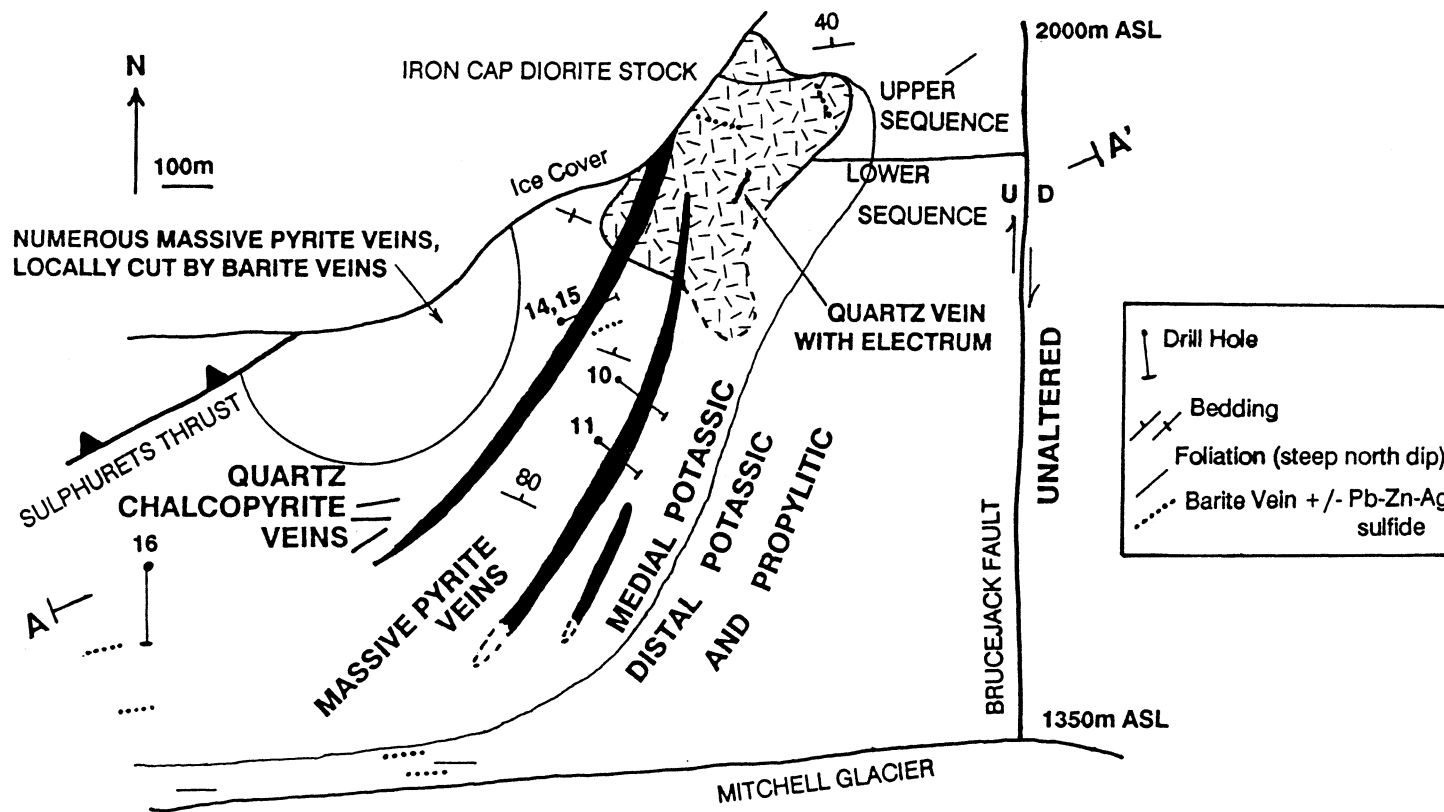


FIGURE 22. Map showing the distribution of hydrothermal alteration and vein types in the Iron Cap subdistrict; note the increasing elevation from south to north; drill hole 16 penetrated quartz-syenite below 170 meters beneath the elevation of the collar of the hole (about 1500 meters); note the unconformity between steeply-dipping Lower Sequence rocks and the more gently-dipping Upper Sequence; cross-section A-A' is shown in Figure 23.

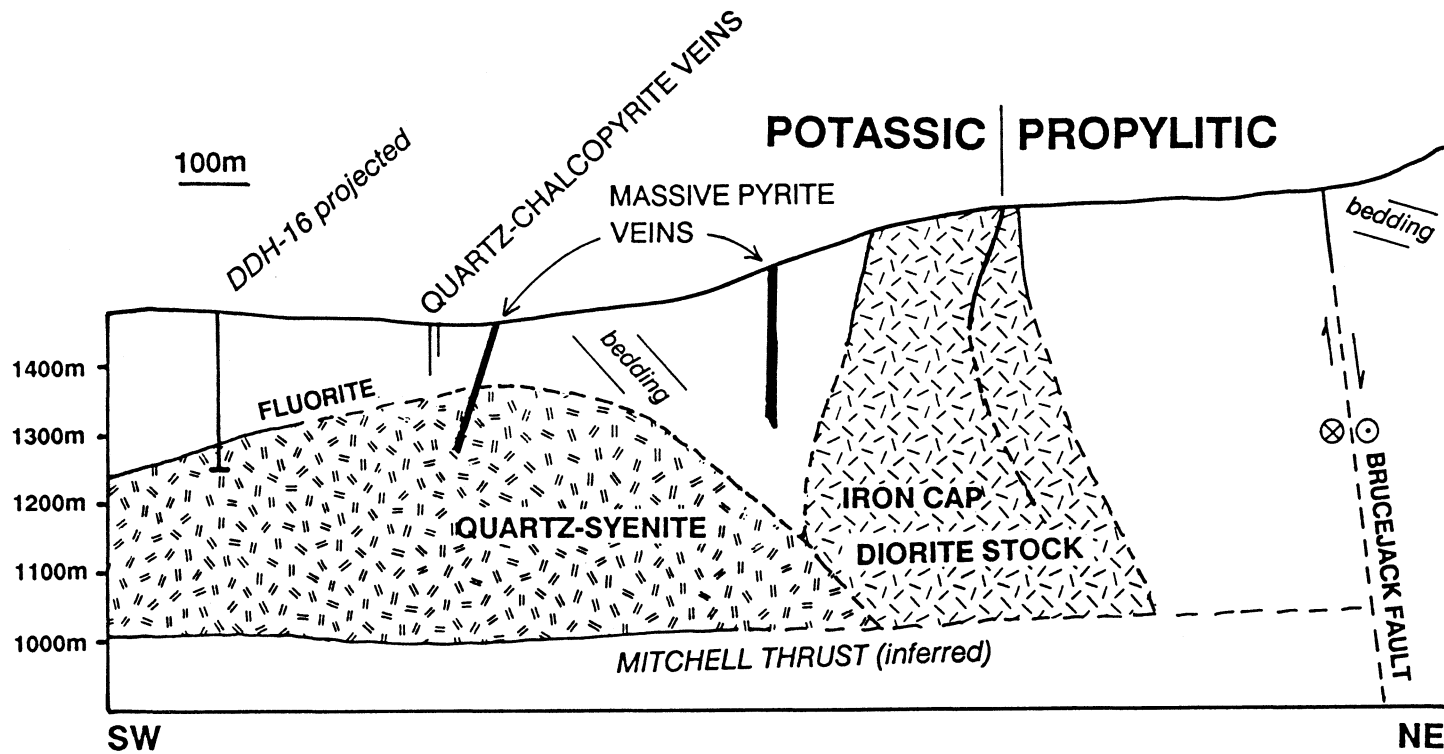


FIGURE 23. Cross-section looking northwest across the western part of the Iron Cap subdistrict; cross-section A-A' in Figure 22; the east side of the Brucejack fault has moved toward the viewer as indicated by the dot-filled circle; the quartz-syenite is shown cutting the pre-mineralization diorite stock, although the shape of these bodies at depth is not known; similarly, the trace of the potassic-propylitic boundary at depth is not known.

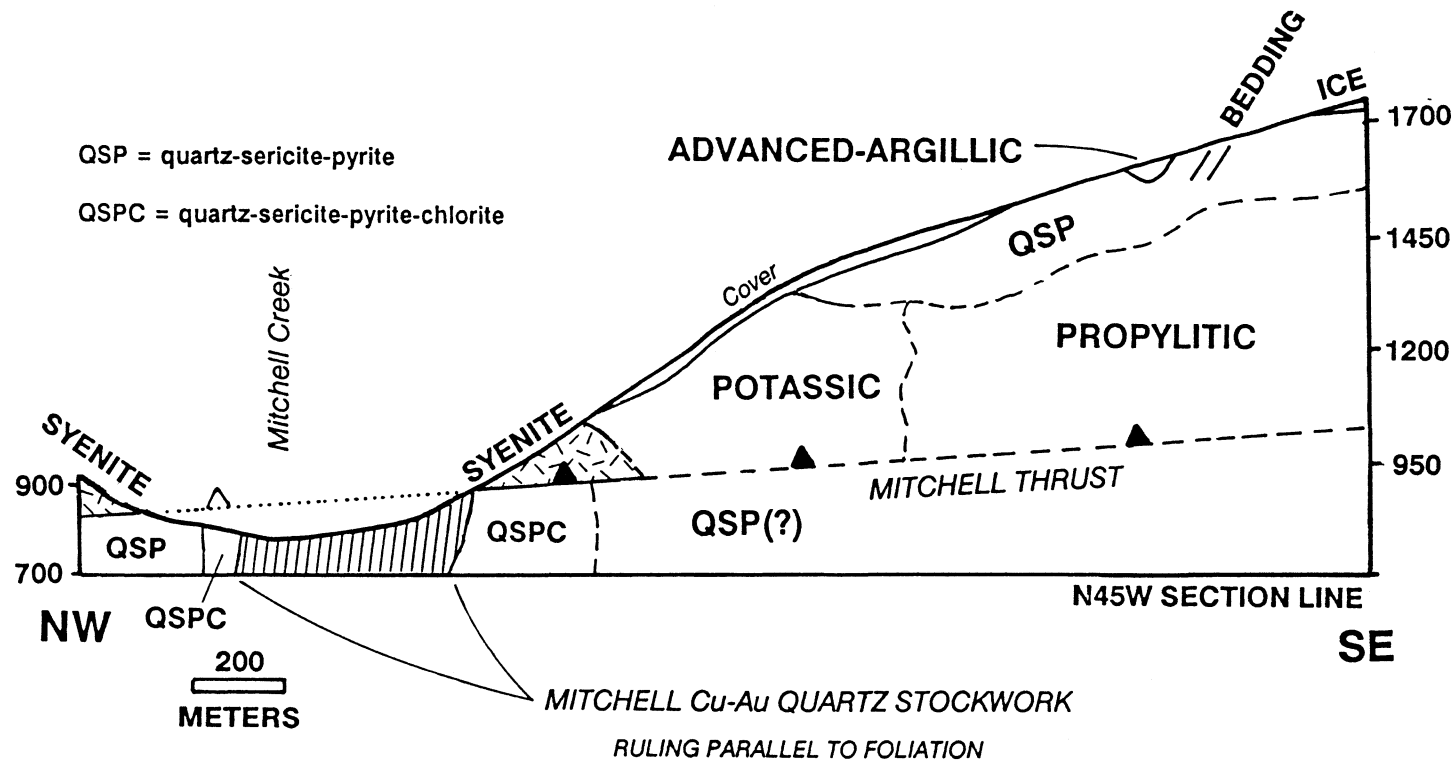


FIGURE 24. Cross-section looking northeast across the western part of the study area, including the eastern Mitchell and western Snowfield subdistricts; see Figures 20 and 21 for cross-section location; elevations above sealevel are in meters; note the location of advanced-argillic alteration at high levels relative to potassic alteration and quartz-syenite, and the truncation of the Mitchell stockwork by the Mitchell thrust.

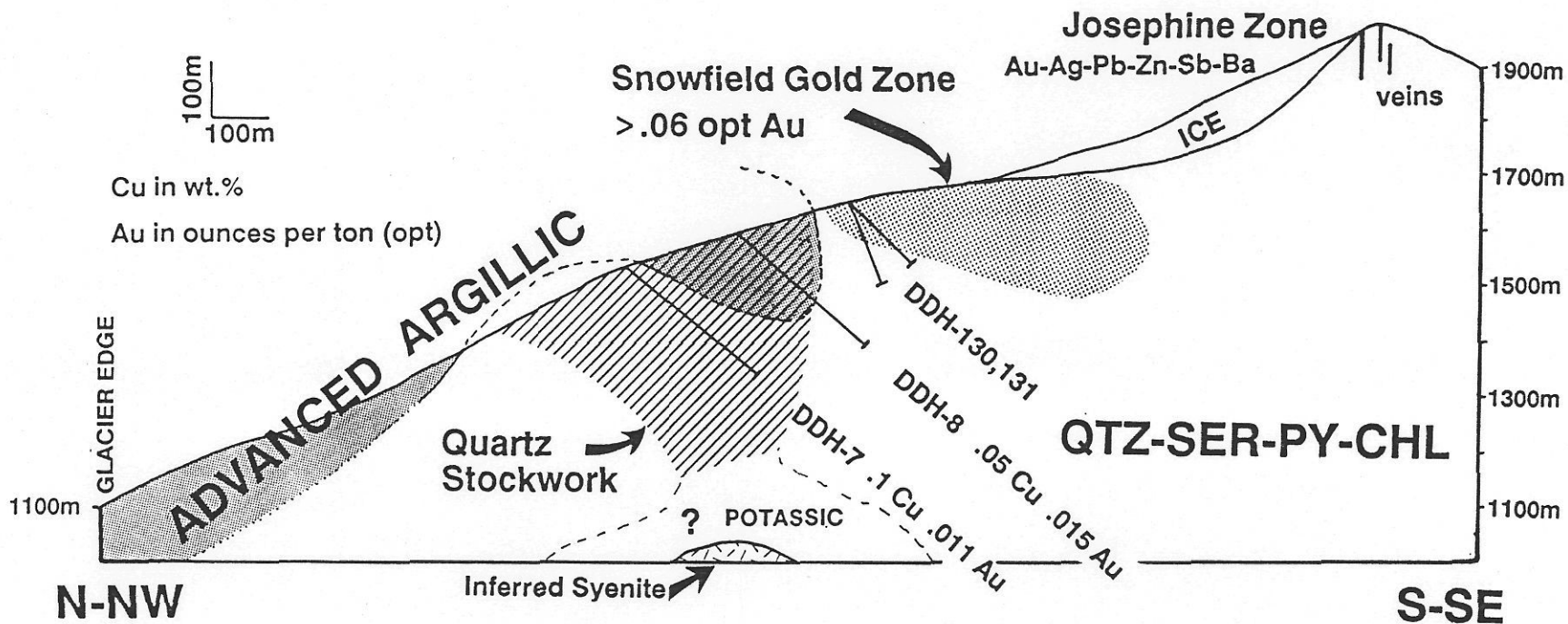


FIGURE 25. Cross-section looking east-northeast across the eastern Snowfield subdistrict; see Figure 20 for location of section line; note the inferred quartz-syenite and preserved potassic alteration at depth, as indicated by the distribution of alteration and quartz-syenite to the west (Figures 20 and 24); the high-grade portion of the Snowfield gold deposit is projected beneath the ice to the south, but the distribution of the mineralization in this area is not known; note the conical shape of the quartz stockwork, the distribution of advanced-argillic alteration, and the high and peripheral, Au-rich Josephine veins.

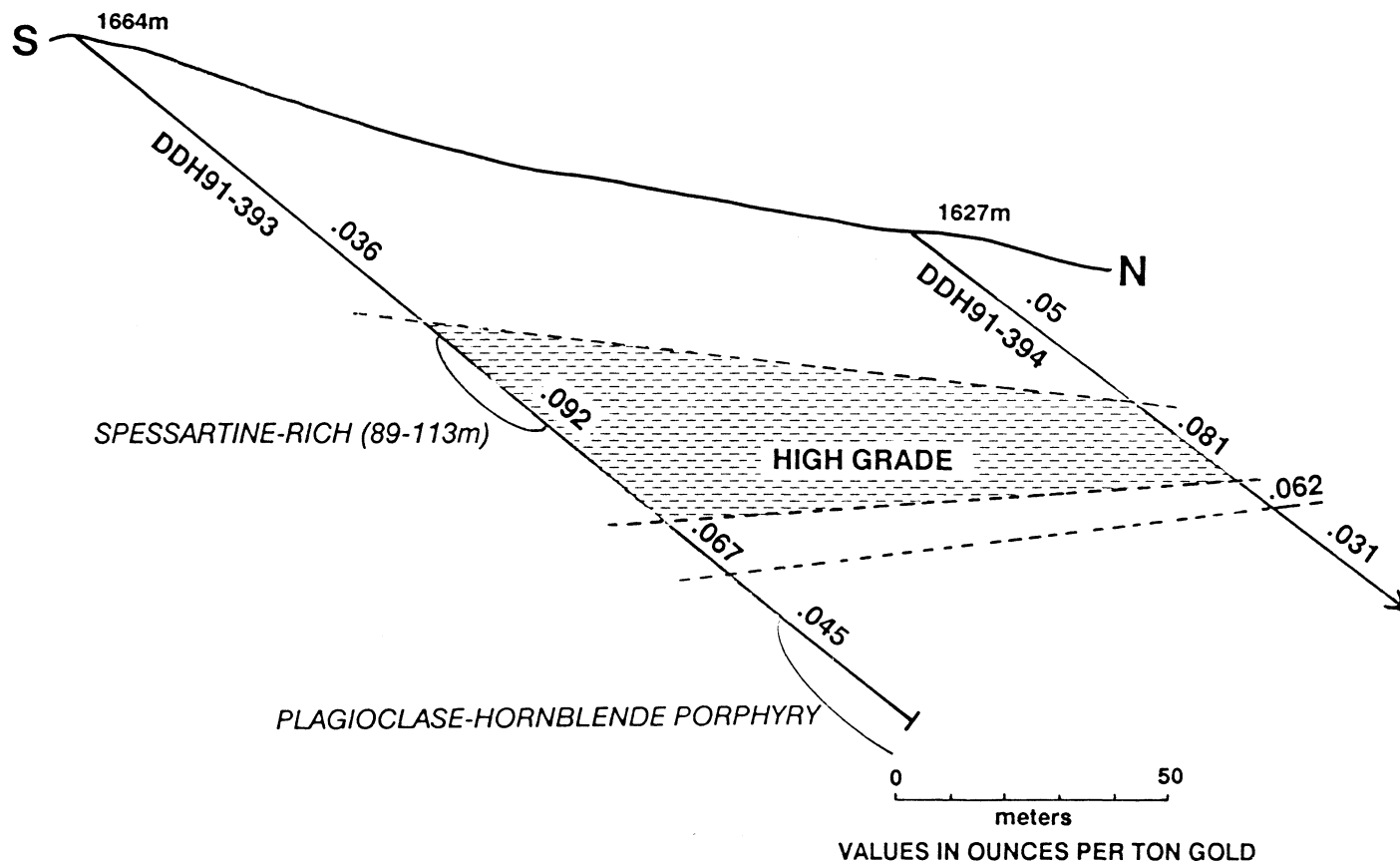


FIGURE 26. Cross-section looking west along the western side of the Snowfield gold zone showing the distribution of gold grades, the tabular nature of the mineralization, the distribution of spessartine garnet, and the dioritic(?) intrusion at depth; no vertical exaggeration; see Appendix H for drill hole data and Map 1 for locations of drill holes.

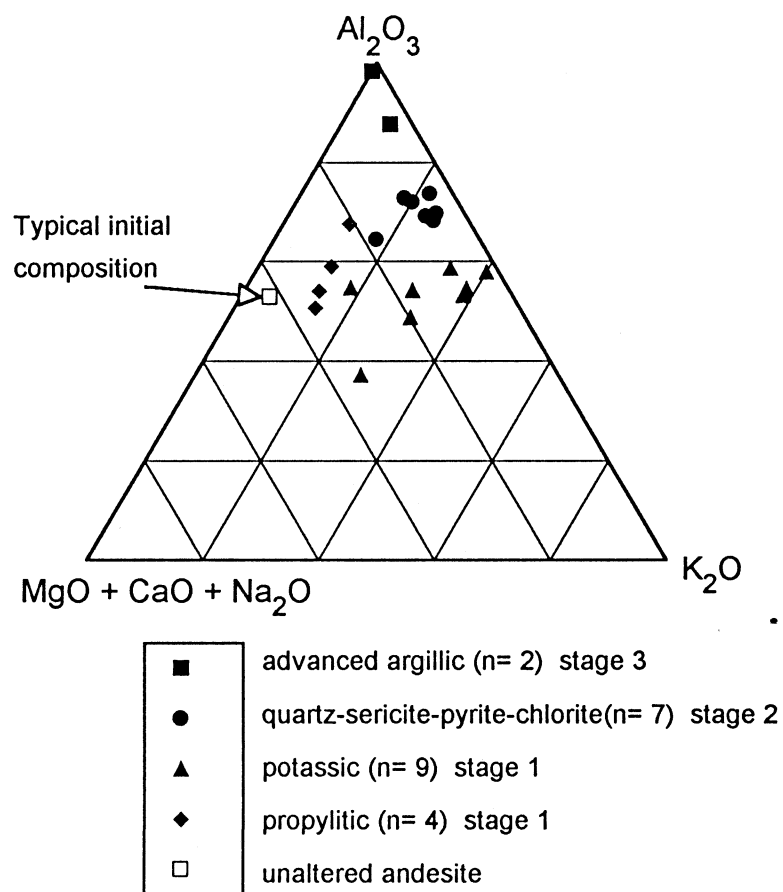


FIGURE 27. Ternary plot of major-oxide compositions of alteration types in the study area; refer to Appendix F for complete analyses; "typical initial composition" is average andesite of Le Maitre (1976).

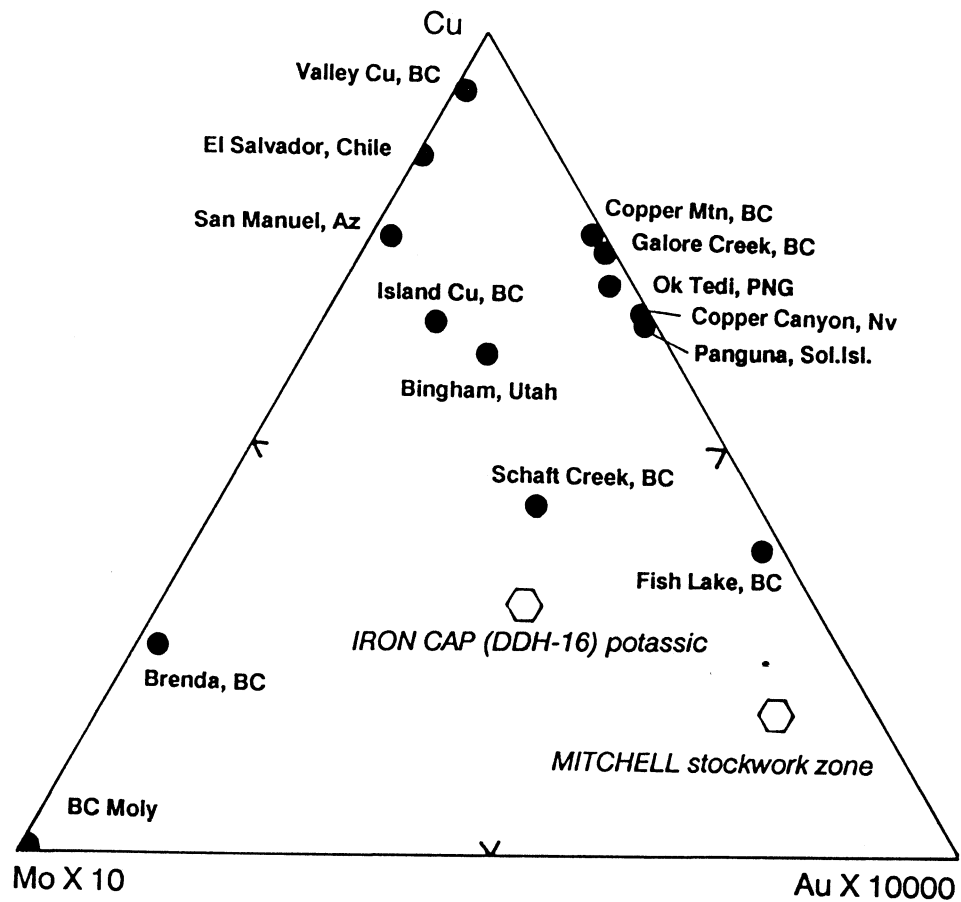


FIGURE 28. Ternary plot of the Cu, Au, and Mo grade of porphyry-type deposits compared to stage-1 mineralization in the study area following the technique of Kesler (1973); data from Kesler (1973), Titley (1978), and Sinclair et al. (1982); note that the size of deposits is not shown by the diagram; abbreviations are: BC, British Columbia; PNG, Papua New Guinea; Nv, Nevada; Az, Arizona; and Sol.Isl., Solomon Islands.

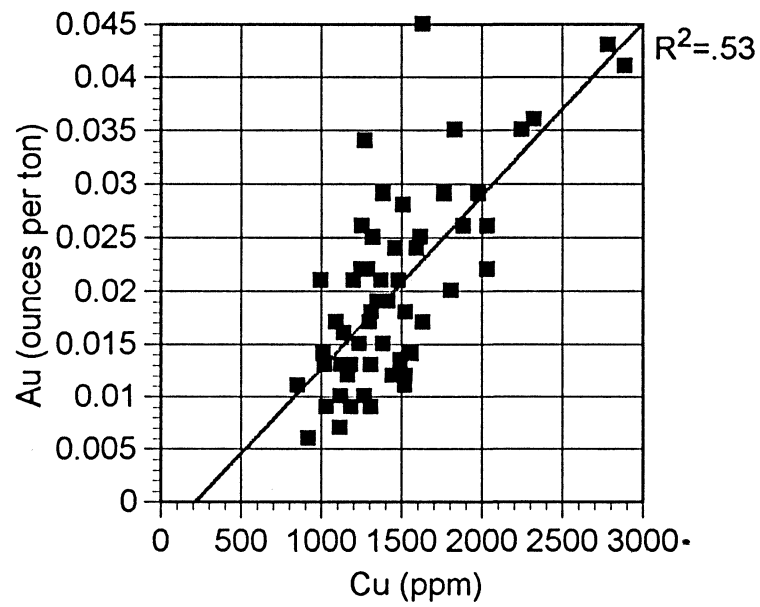


FIGURE 29. Plot of Au versus Cu for 3-meter assay intervals in drill hole DDH-387 in the Mitchell quartz stockwork; the correlation coefficient, R^2 , is .53; refer to Appendix H for drill hole information.

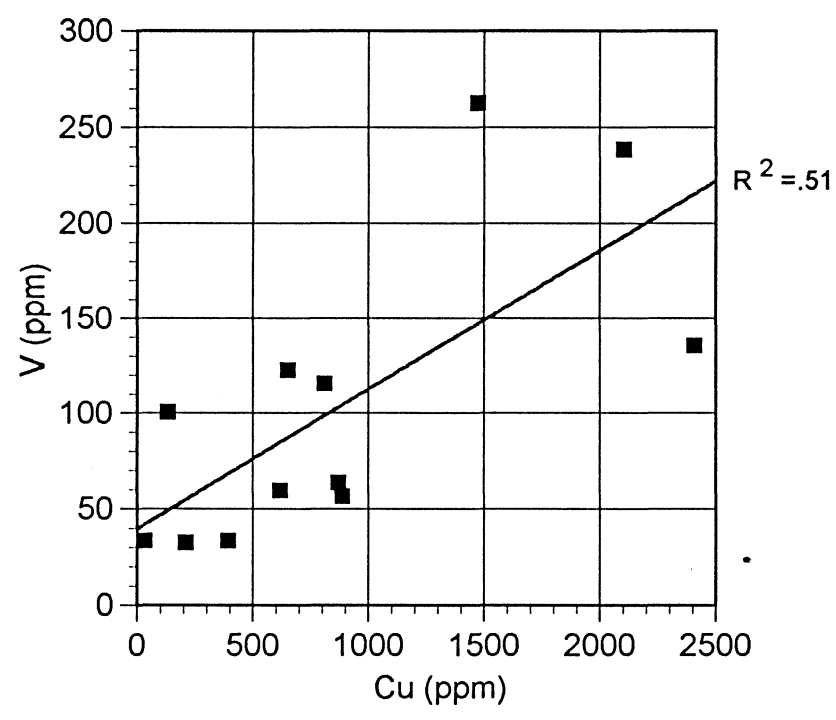


FIGURE 30. Plot of V versus Cu for 12 potassically-altered rocks in the study area for which trace-element data are available; the correlation coefficient, R^2 , is .51.

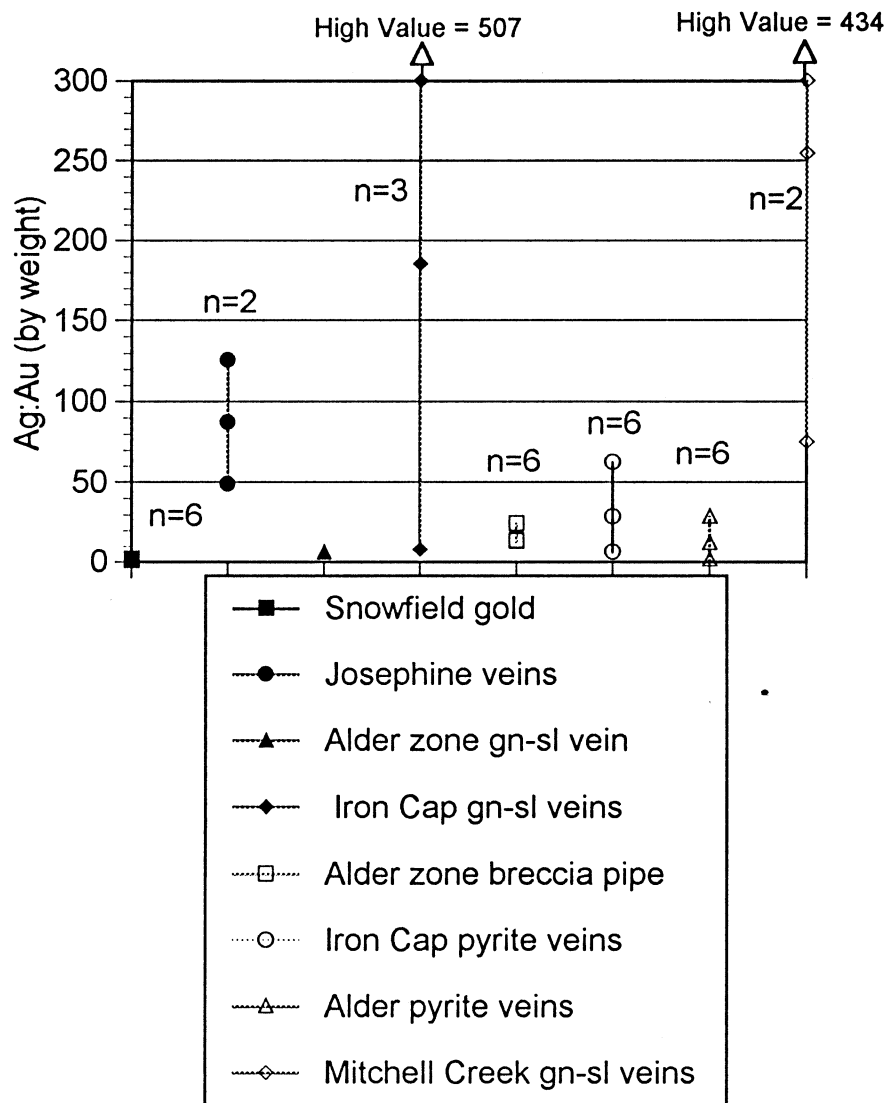


FIGURE 31. Ratios of Ag-to-Au by weight for stage-4 mineralization in the study area as shown in the legend; values along each bar represent the low, average, and high values for the given group; note the distinctly low ratio for the Snowfield gold deposit as discussed in the text; gn, galena; sl, sphalerite.

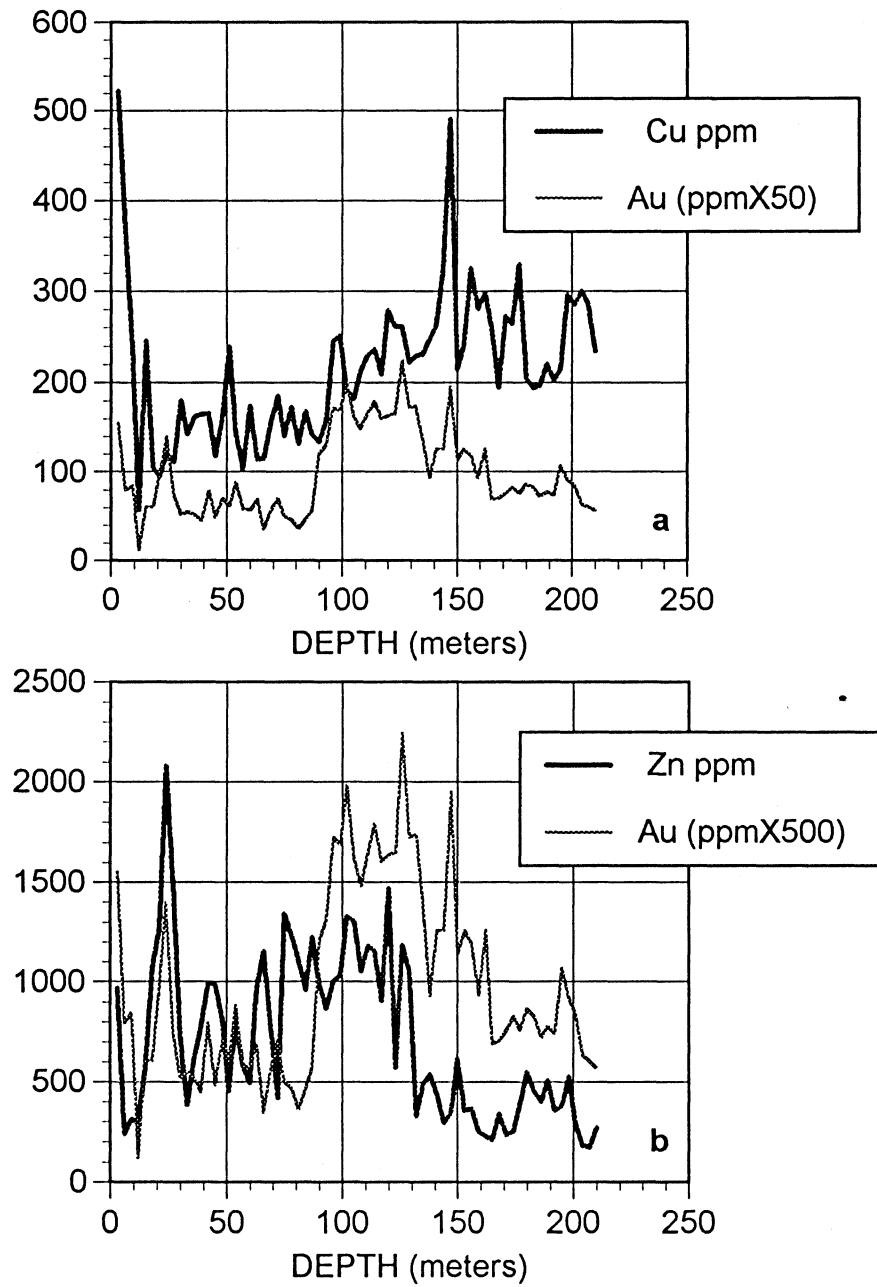


FIGURE 32. Plots of metal enrichments versus approximate depth in drill hole DDH-393 in the western part of the Snowfield gold deposit; 3-meter assay intervals; (a), Cu and Au; (b), Zn and Au.

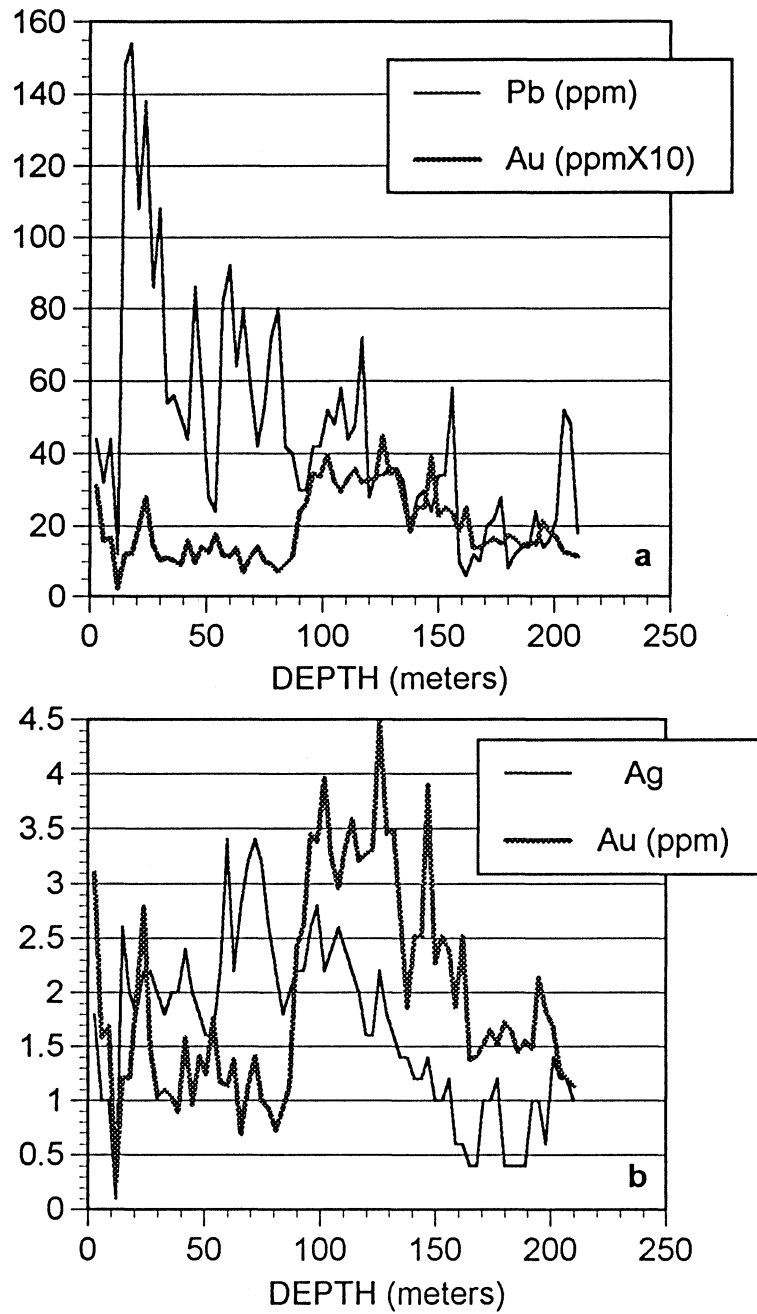


FIGURE 33. Plots of metal enrichments versus approximate depth in drill hole DDH-393 in the western part of the Snowfield gold deposit; 3-meter assay intervals; (a), Pb and Au; (b), Ag and Au.

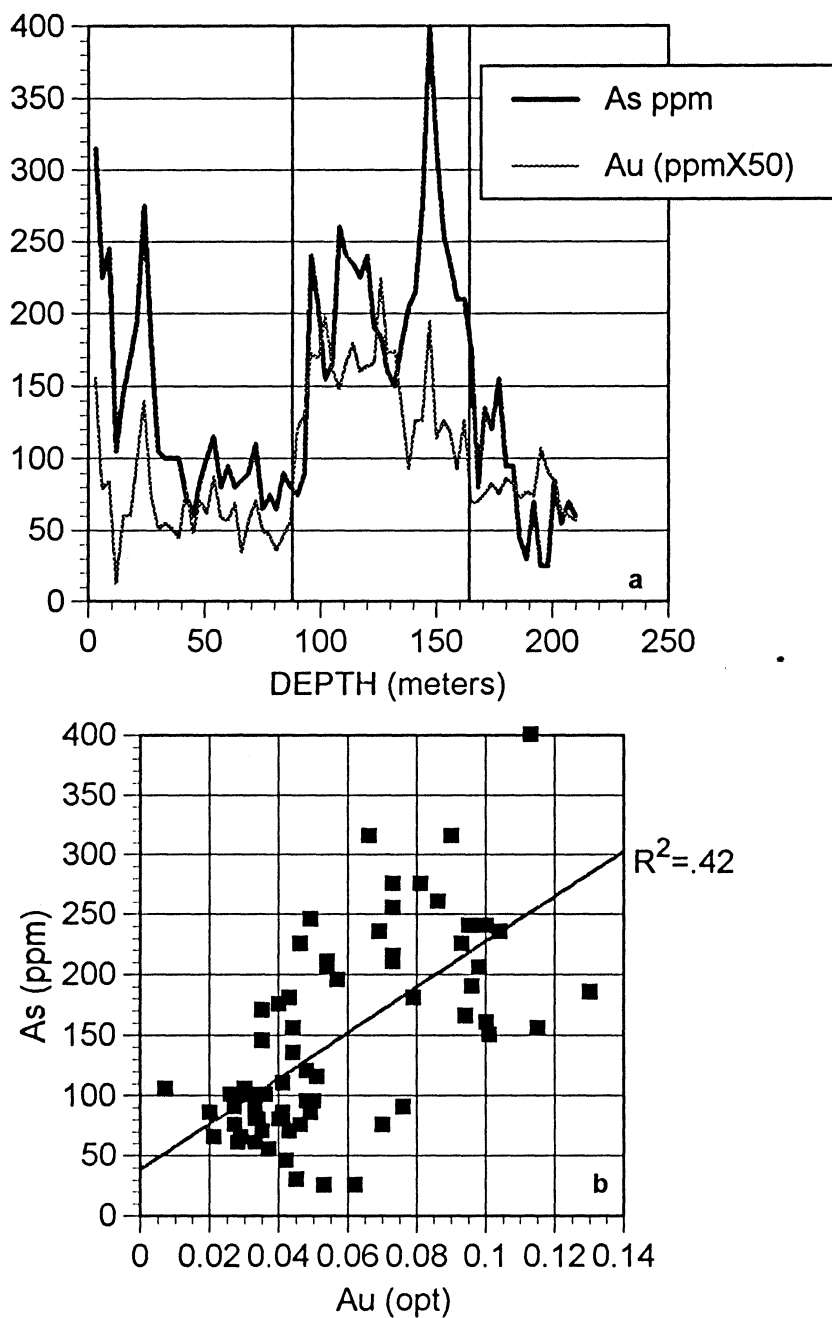


FIGURE 34. (a) Plot of Au and As versus approximate depth in drill hole DDH-393 (3-meter assay intervals) in the western part of the Snowfield gold deposit, vertical lines delineate high-grade wedge; (b) Plot of Au versus As for DDH-393 showing a positive correlation, $R^2 = .42$; drill hole 394 (see Figure 26) has an As-Au correlation of .54.

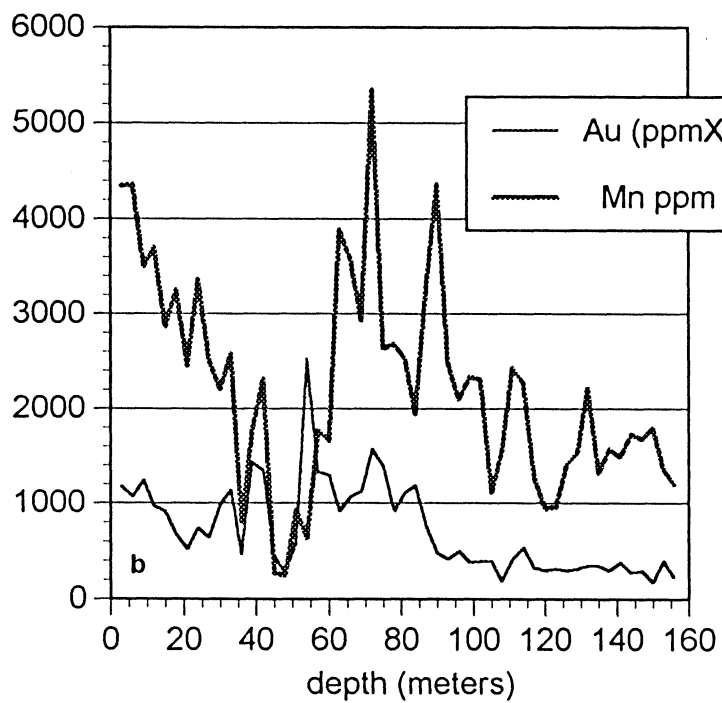
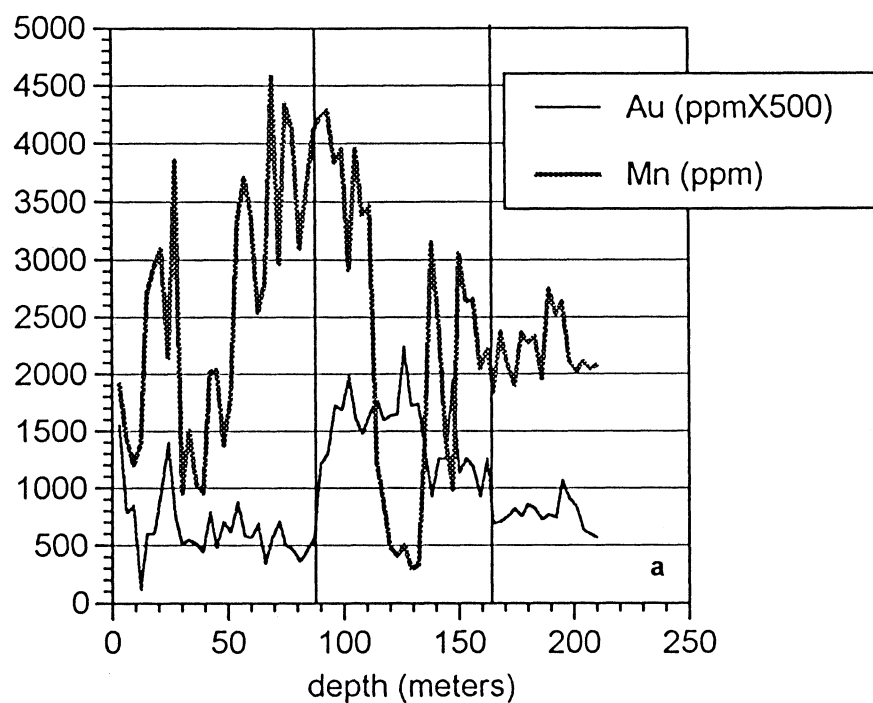


FIGURE 35. Plots of Mn and Au versus depth in drill holes DDH-393 (a) and DDH-394 (b); 3-meter assay intervals; high-grade Au wedge delineated in (a) by vertical lines; note sharp decrease in Mn in center of high-grade interval.

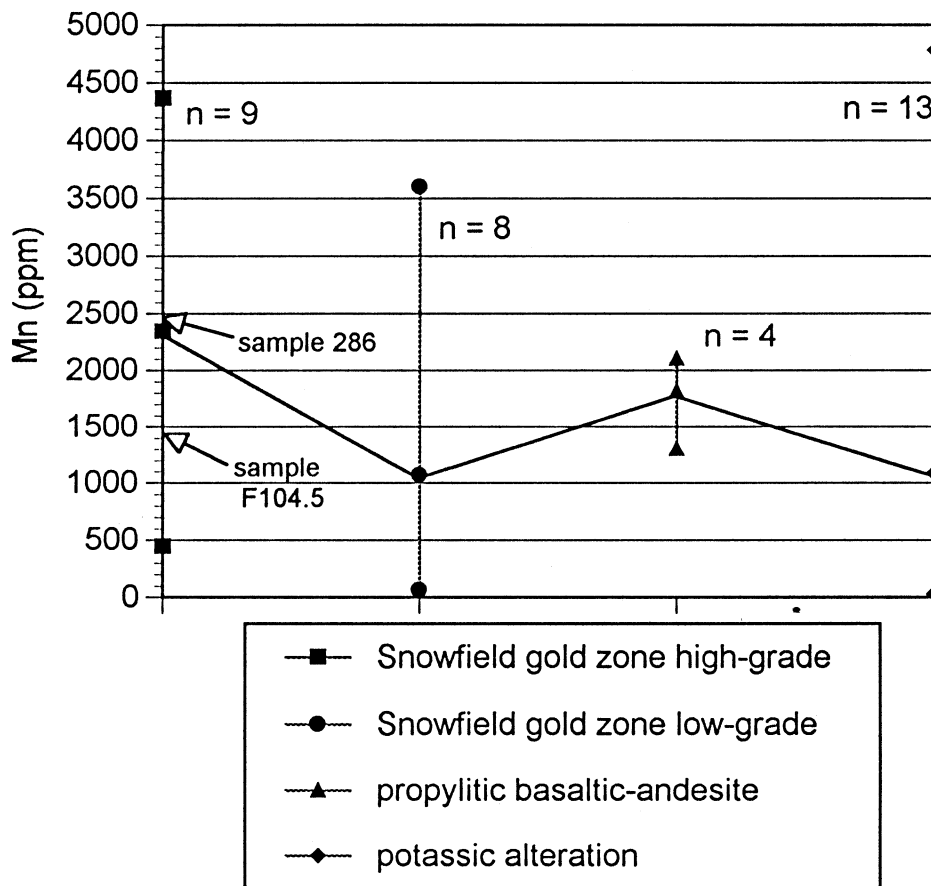


FIGURE 36. Concentration of Mn in Snowfield gold zone and propylitic and potassic alteration elsewhere in the study area; values for each bar are the low, average, and high values; note the higher average Mn contents in the high-grade zone (500 ppm higher than other alteration types) even though spessartine garnet is locally present in areas not significantly enriched in Mn (see text); high-grade samples used in this plot that contain spessartine are shown with arrows pointing to their Mn values (see Appendix B, surface sample 286 [.13 opt Au] and sample F104.5 [.10 opt Au, 104.5m depth in DDH-393]).

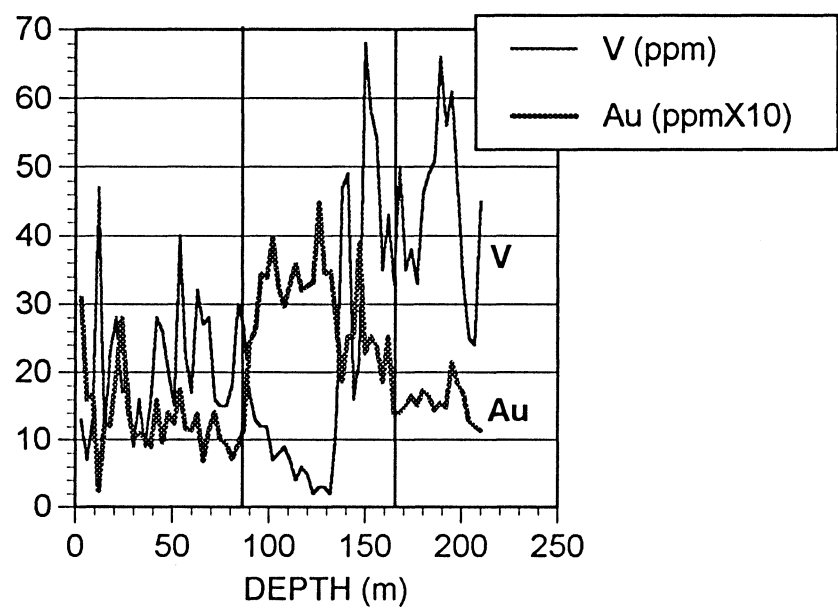


FIGURE 37. Plot of V and Au versus approximate depth in Snowfield gold zone drill hole DDH-393; 3-meter assay intervals; note the lower V contents in the higher-grade gold mineralization, delineated by vertical lines.

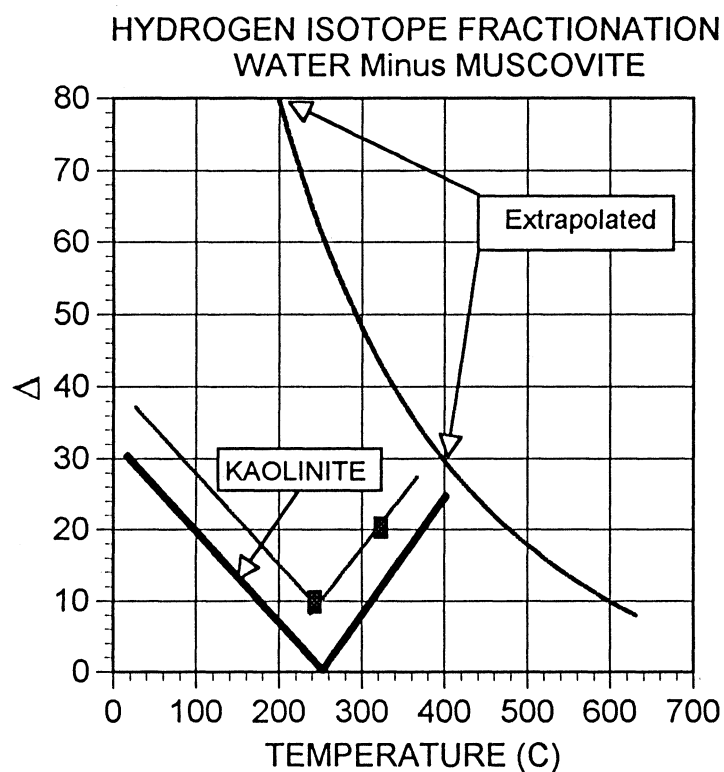


FIGURE 38. Plot of temperature versus the per-mil difference (Δ) in hydrogen isotope composition between water and muscovite; the smooth curve is for water-muscovite extrapolated below 450°C from Suzuoki and Epstein (1976), and is referred to as the "extrapolation method" in the text; the heavy V-shaped curve is that for water minus kaolinite, and the lighter V-shaped curve is that assumed for water-muscovite by Lambert and Epstein (1980) and others (see text) based on the two actual analyses from active hydrothermal areas (filled rectangles); use of the V-shaped muscovite curve is referred to as the "kaolinite method" in the text.

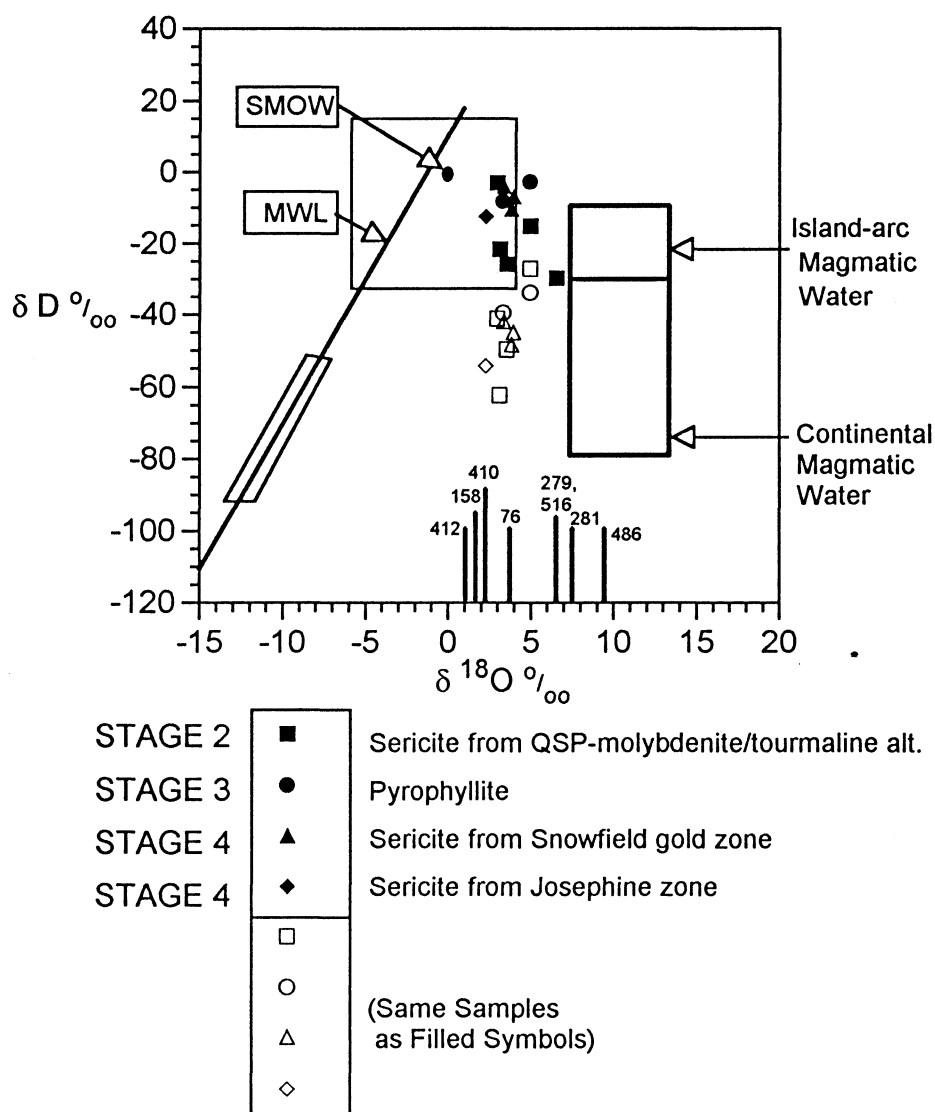


FIGURE 39. Isotopic composition of hydrothermal fluids as calculated from the sample analyses; see Table 5 for data; SMOW is the reference "standard mean ocean water", MWL is the world-wide meteoric water line of Craig (1961), large box is the field of fluid-inclusion fluid compositions from Kuroko-type deposits (Pisutha-Arnond and Ohmoto (1983); narrow rectangle along MWL is the assumed composition of Lower Jurassic meteoric waters at Sulphurets; vertical lines are quartz samples (no δD data; 486, stage-1 quartz-magnetite vein; 76, 279, 516, 281, stage-1 quartz stockworks; 410, 158, 412, stage-4 quartz-barite veins); filled and open symbols represent the same set of samples in Table 5 calculated using the extrapolation and kaolinite methods, respectively; the filled square with the highest $\delta^{18}O$ value is shared by both methods; see text for further discussion.

FIGURE 40. Plot of the hydrogen and oxygen isotopic composition of sericites and some pyrophyllites from magmatic-hydrothermal deposits, largely porphyry Cu-Mo systems; polygon outlines samples from deposits which formed in oceanic islands (Waisoi, Pueblo Viejo, Koloula, Ok Tedi, Panguna, Kuroko) or formed during island-arc magmatism in accreted island-arc terranes (Sulphurets, Highland Valley); note that, except for El Salvador and Mineral Park, systems in continental interiors or continental volcanic arcs (e.g., Mt. Tolman) plot distinctly lighter in δD ; data sources are: Pueblo Viejo, Dominican Republic (Vennemann et al., 1993); Pilot Mountain, North Carolina (Klein and Criss, 1988); Climax, Colorado (Hall et al., 1974; Sheppard et al., 1971); Ely, Nevada, Mount Tolman, Washington, Mineral Park, Arizona, Bingham, Utah, and Santa Rita, Arizona (Sheppard et al., 1971; Bowman et al., 1987); El Salvador, Chile (Sheppard and Gustafson, 1976); Ok Tedi, New Guinea, and Koloula, Solomon Islands, and Waisoi, Fiji (Chivas et al., 1984); Panguna, Bouganville (Ford and Green, 1977); Butte, Montana (Sheppard and Taylor, 1974); Highland Valley, British Columbia (Osatenko and Jones, 1976); Kuroko deposits, Japan (Hattori and Muehlenbachs, 1980); Red Mountain, Arizona (Rye, 1993).

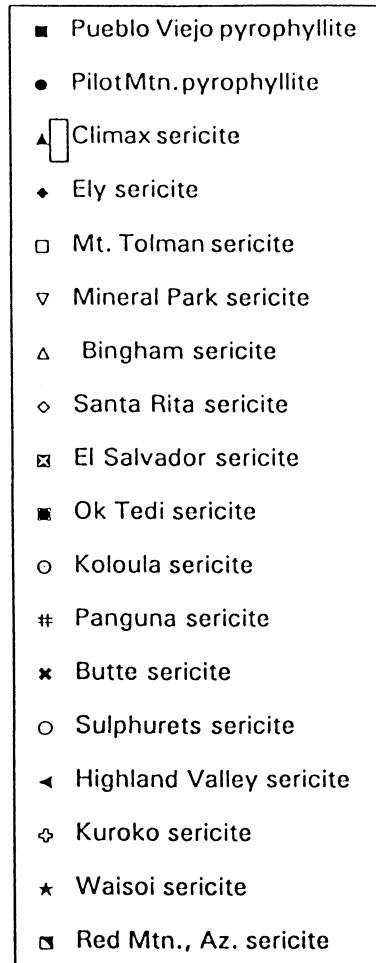
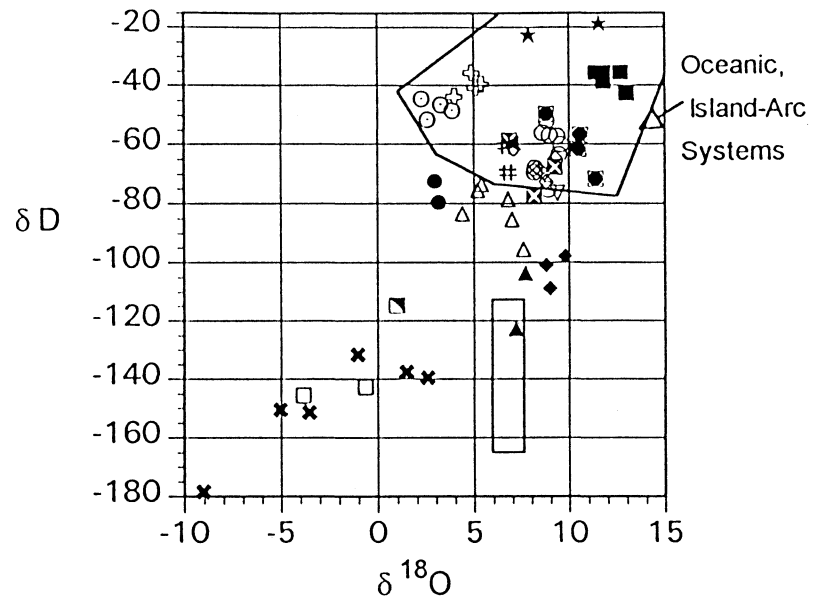


FIGURE 41. Results of CHILLER calculations at 300°C of the reaction between andesite and a 10:1 mixture of seawater and magmatic fluid as discussed in Chapter VIII; log moles of minerals are plotted with respect to the amount of andesite in grams added to 1 kilogram of the fluid, decreasing w/r from left to right; A shows gangue minerals and B shows additional minerals between 100 and 1000 grams of andesite added (note the different scale for the abscissa); C shows "ore" minerals, with the abscissa scale as in B; mineral abbreviations are: S, native sulfur; QTZ, quartz; BAR, barite; ANH, anhydrite; PY, pyrite; AL, alunite; PL, pyrophyllite; CL, Mg-chlorite (clinochlore); DAP, Fe-chlorite (daphnite); RHO, rhodonite; MUS, muscovite; HEM, hematite; PAR, paragonite; EP, epidote; CZ, clinozoisite; ALB, albite; COV, covellite; CP, chalcopyrite; SPH, sphalerite; SILV, native silver; note the overlap (with respect to the w/r) between advanced-argillic alteration (alunite and pyrophyllite) and sericitic alteration (muscovite, pyrite) and the fact that both occur at $w/r > 1$; propylitic alteration is represented on the right side of the diagrams by the assemblage albite-chlorite-epidote; the weight percents of minerals at $w/r = 1$ (right edge of figures) are albite (11), anhydrite (4.5), barite (.13), chalcopyrite (.01), Mg-chlorite (10), Fe-chlorite (1.7), epidote (15), clinozoisite (2.5), gold (.00000008), silver (.000000002), hematite (.8), muscovite (7.5), paragonite (12), pyrite (2), quartz (32), rhodonite (.2), and sphalerite (.005).

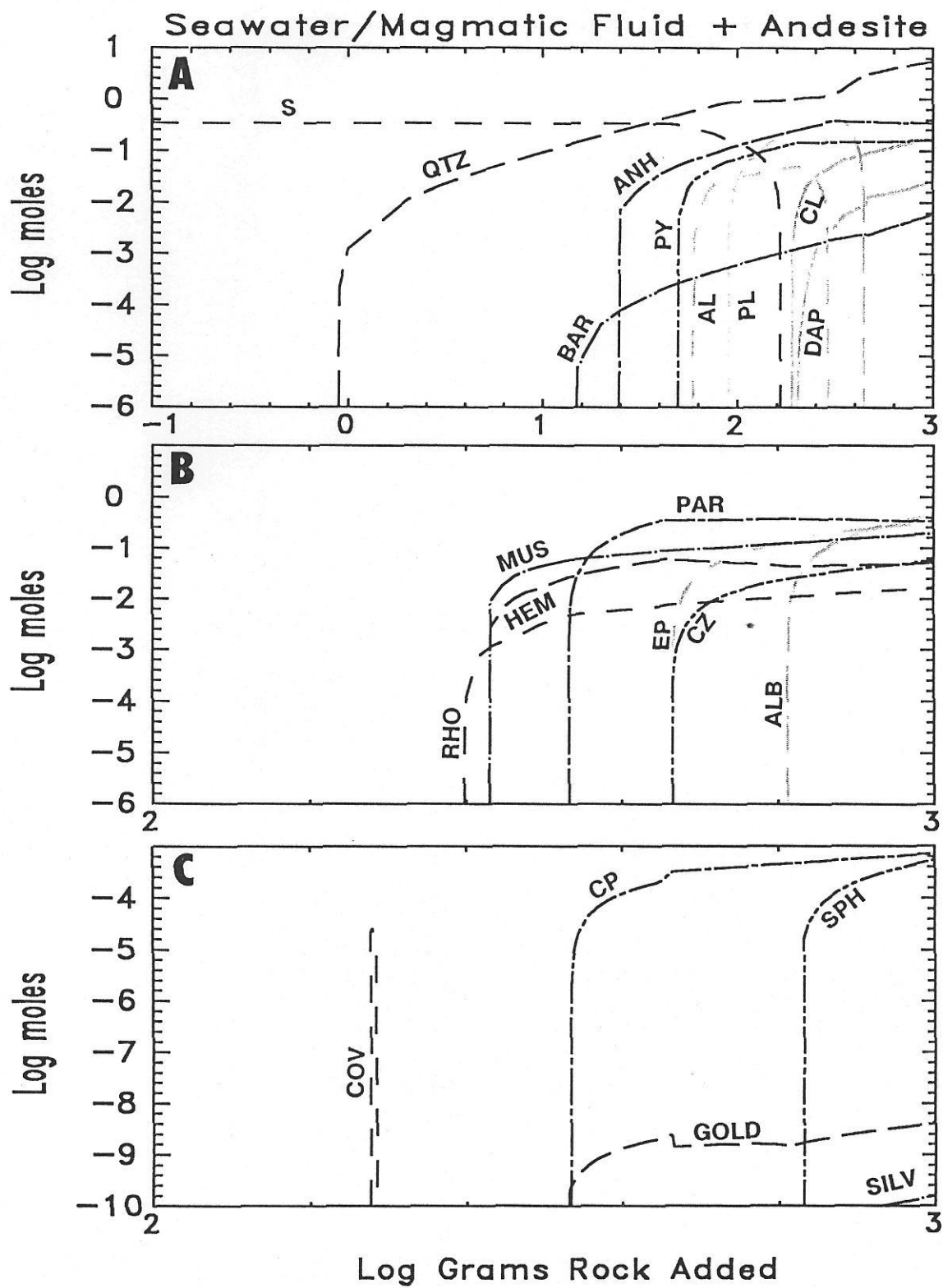
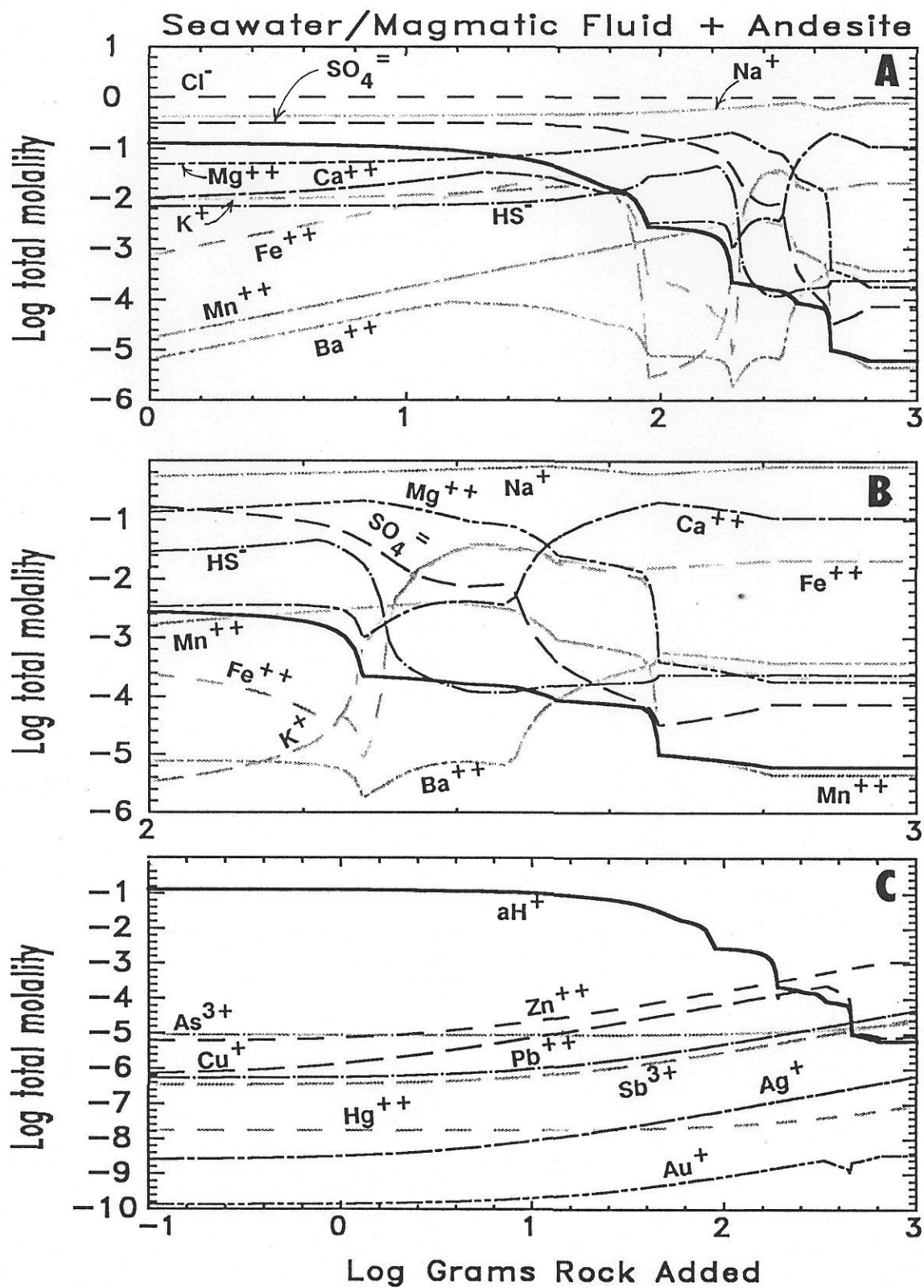


FIGURE 42. Concentrations of aqueous components (total concentration) in molality (moles per kilogram of water) calculated from the reaction discussed in Chapter VIII (see Figure 41); note the different abscissa scales for each diagram, chosen to clarify the concentration curves; diagram B is a magnification of the right part of diagram A, and diagram C shows metal species; the heavy line in each diagram is the $\log aH^+$ (negative pH); note the increasing concentrations of metals by as much as two orders of magnitude with increasing reaction (decreasing w/r from left to right) indicating that metals are leached from the rock; note that, although the initial total sulfate ($SO_4^{=}$) concentration is one order of magnitude greater than the total sulfide (HS^-) concentration and sulfide declines during the reaction due to precipitation of sulfide minerals, that sulfide dominates in the propylitic facies; the reaction simulating the formation of the Snowfield gold deposit (Chapter IX) uses the fluid from this reaction at the point of highest sulfide concentration (log 2.2 grams rock added).



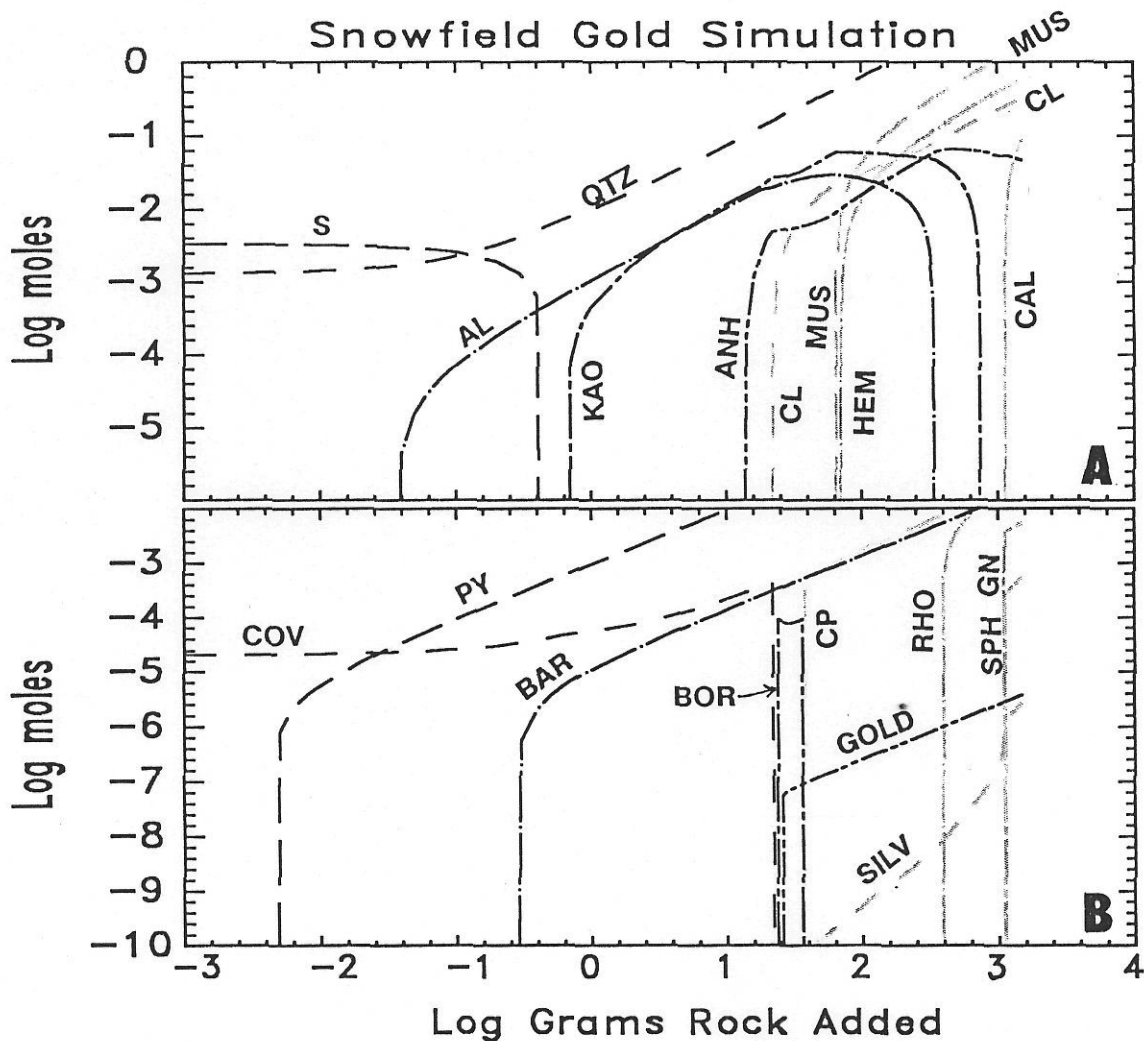
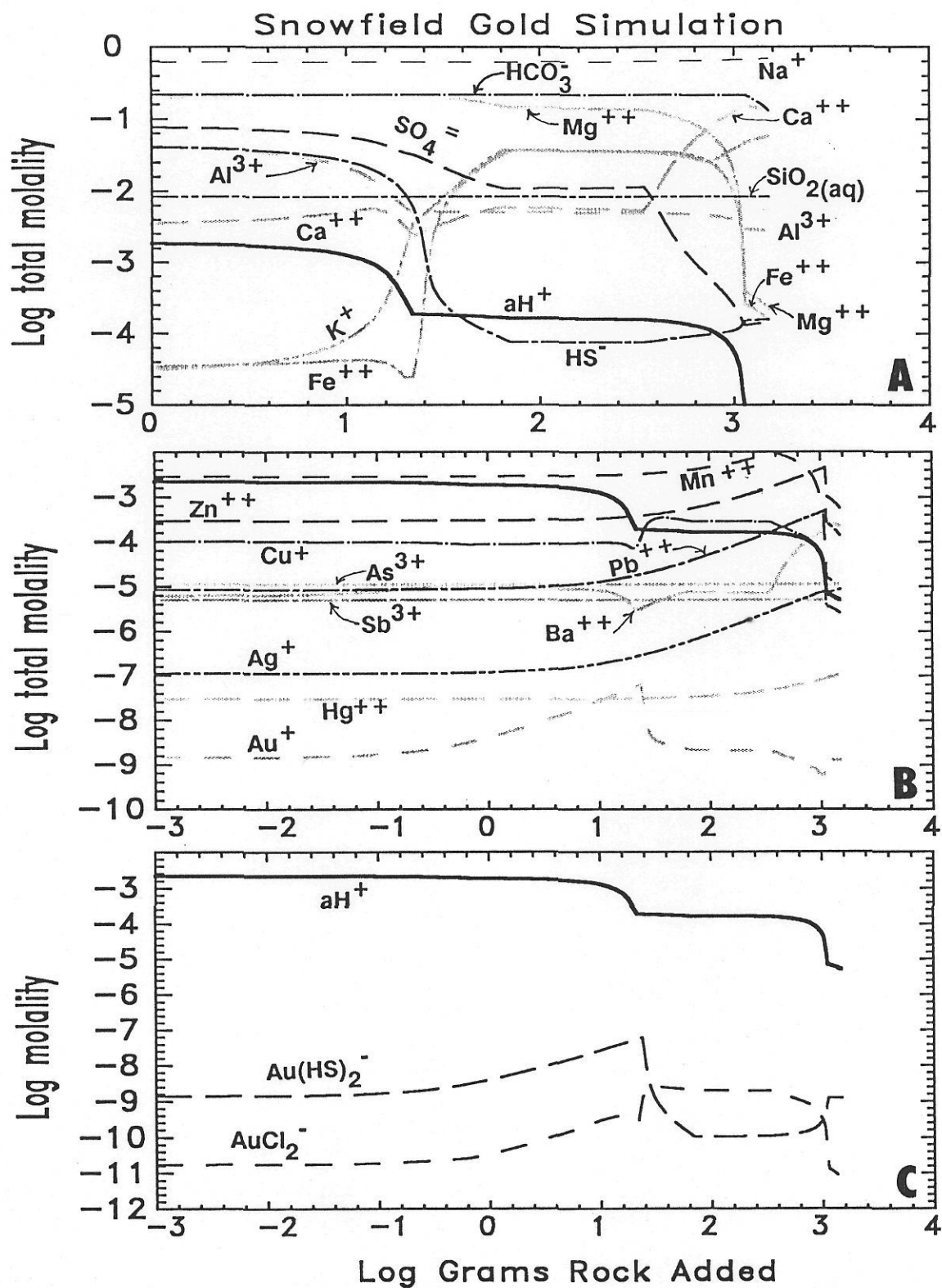


FIGURE 43. Minerals calculated from the numerical reaction at 280°C attempting to simulate the formation of the Snowfield gold deposit as discussed in Chapter IX; diagram A shows gangue minerals, B shows sulfides and metal-bearing phases; decreasing w/r from left to right; abbreviations as in Figure 41 with the addition of KAO (kaolinite), CAL (calcite), BOR (bornite), and GN (galena); note that an advanced-argillic facies is replaced by muscovite-chlorite-quartz at decreasing w/r and that this change is accompanied by the precipitation of electrum, galena, sphalerite, chalcopyrite, and rhodonite with barite; at the end of the reaction (right edge) at 1500 grams of rock added (w/r=.67), the weight-percents of minerals are: quartz (36), Mg-chlorite (12), Fe-chlorite (2), muscovite (41), hematite (6), anhydrite (.4), barite (.3), calcite (.6), galena (.008), sphalerite (.04), rhodonite (.25), pyrite (.5), chalcopyrite (.4), gold (.518 ppm), and silver (.193 ppm).

FIGURE 44. Concentrations of aqueous species in moles per kilogram water versus grams of rock added for the reaction simulating the formation of the Snowfield gold deposit as discussed in Chapter IX; diagrams A and B show total concentrations of component species, and C shows the concentrations of the significant, individual gold complexes and HS^- ; the heavy line in each diagram is negative pH; note the different scale for the abscissa in diagram A.



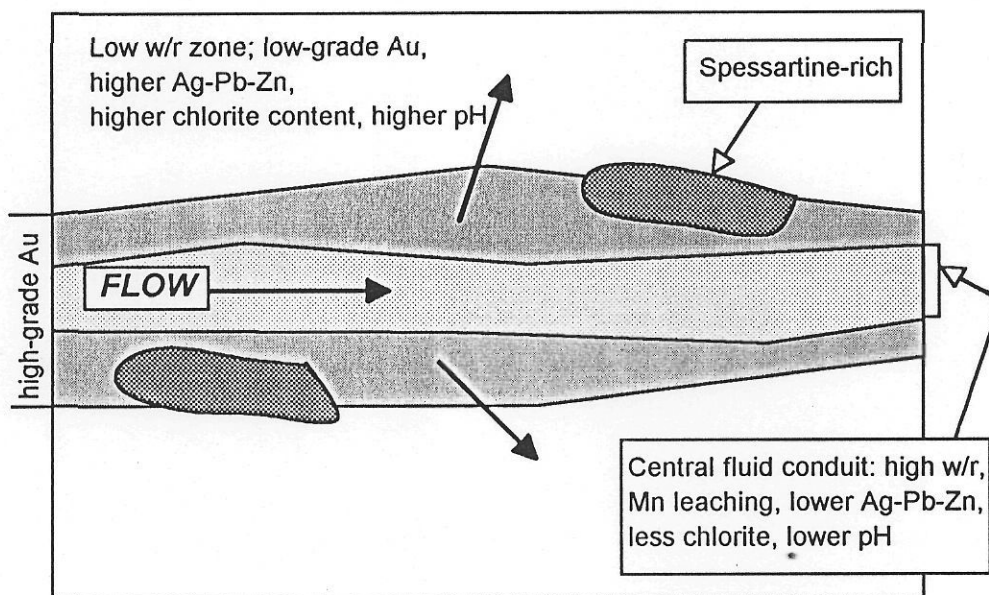


FIGURE 45. Schematic model for the formation of the Snowfield gold deposit as discussed in the text; heavy arrows represent fluid flow; diagram represents about 100 meters in the vertical dimension.

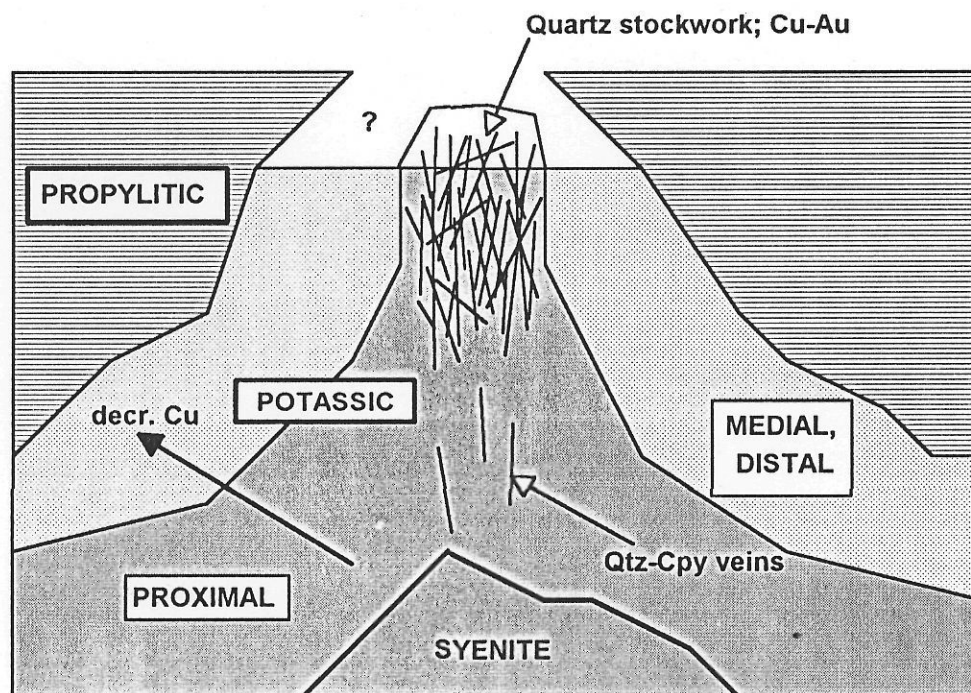


FIGURE 46. Schematic model of the hydrothermal system during stage 1 as discussed in the text; question mark indicates a lack of information concerning the uppermost part of the system during stage 1; narrow lines are quartz veins.

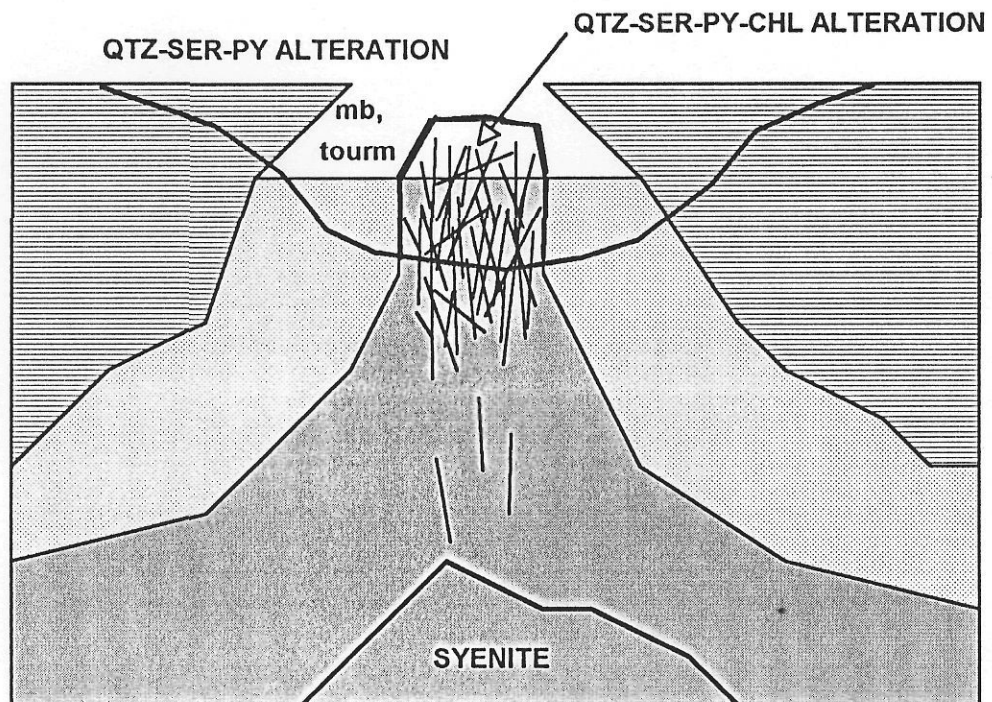


FIGURE 47. Schematic model of the hydrothermal system during stage 2 as discussed in the text; thick line marks the lower limit of the bulk of stage-2 alteration; abbreviations: qtz, quartz; ser, sericite; py, pyrite; chl, chlorite; mb, molybdenite; tourm, tourmaline.

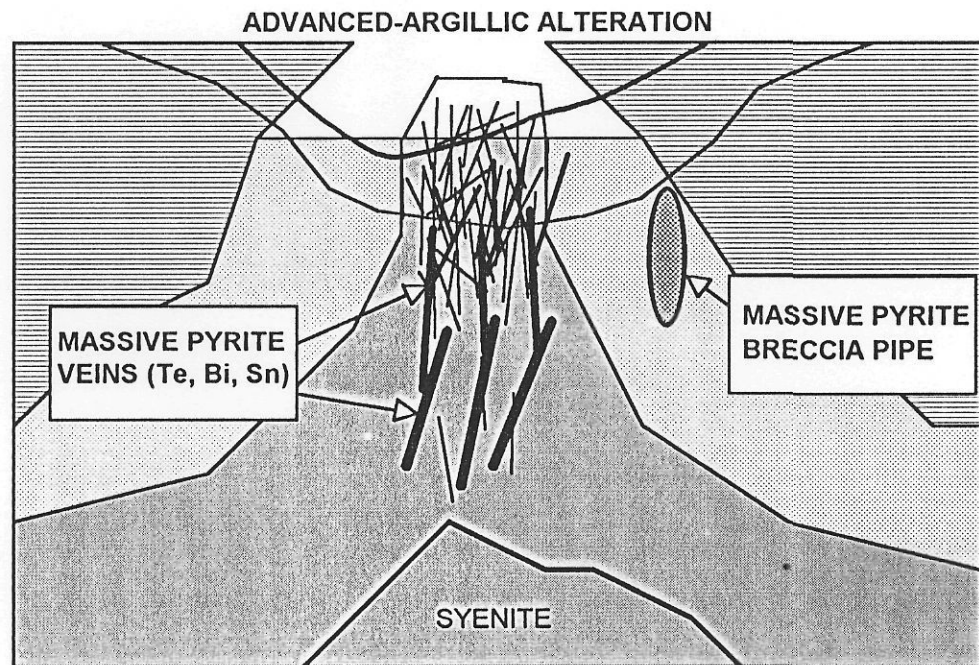


FIGURE 48. Schematic model of the hydrothermal system during stage 3 as discussed in the text; short thick lines (veins) are massive pyrite; thick line near the top of the figure marks the lower limit of advanced-argillic alteration.

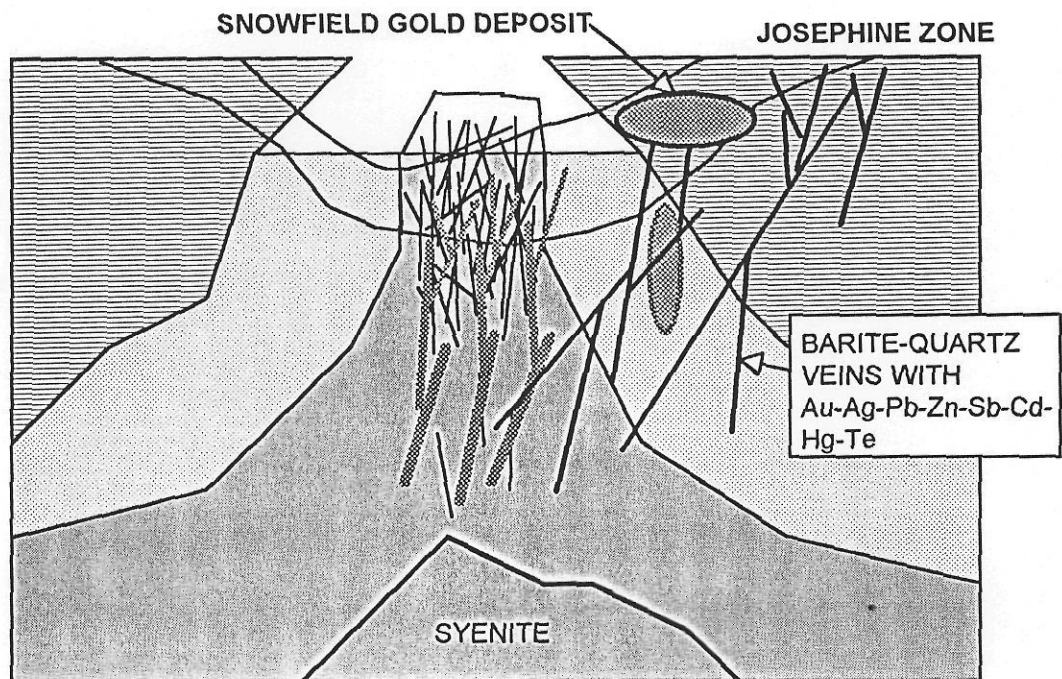


FIGURE 49. Schematic model of the hydrothermal system during stage 4 as discussed in the text; shaded veins are stage-3 massive pyrite.

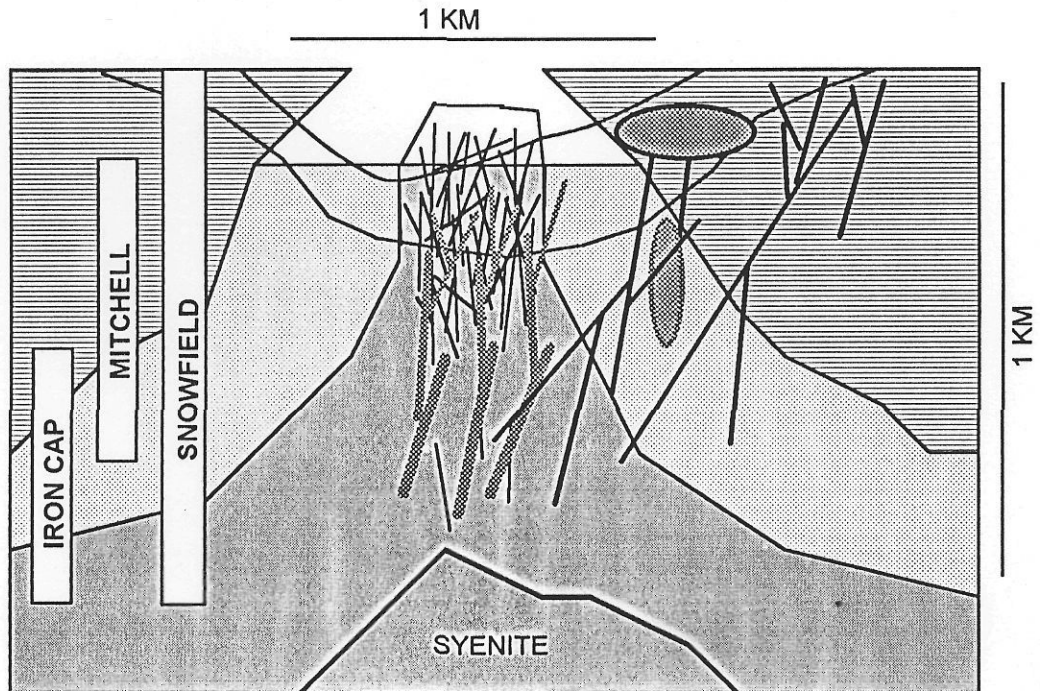


FIGURE 50. Schematic model of the hydrothermal system as in Fig. 49 showing which parts of the system are present in the three subdistricts as shown along the left side of the figure; also note the approximate vertical and horizontal scales.